Detailed analysis of chick optic fissure closure reveals Netrin-1 as an essential mediator of epithelial fusion

Detailed analysis of chick optic fissure closure reveals Netrin-1 as an essential mediator of epithelial fusion.

Hardy H[1], Prendergast J[1], Patel A[2], Dutta S[4], Trejo-Reveles V[1], Kroeger H[1], Yung A[3], Goodrich L[3], Brooks BP[4], Sowden J[2], and Rainger J[1*]

1. The Roslin Institute and R(D)SVS, University of Edinburgh, Easter Bush Campus, Midlothian, UK. EH25 9RG
2. Birth Defects Research Centre, UCL Great Ormond Street Institute of Child Health, 30 Guilford Street, London, WC1N 1EH, UK
3. Department of Neurobiology, Harvard Medical School, 220 Longwood Avenue, Boston, MA 02115, USA
4. Ophthalmic Genetics and Visual Function Branch, National Eye Institute, National Institutes of Health, Bethesda, MD 20892, USA

* Corresponding author: joe.rainger@roslin.ed.ac.uk

ABSTRACT.

Epithelial fusion underlies many vital organogenic processes during embryogenesis. Disruptions to these cause a significant number of human birth defects, including ocular coloboma. We provide robust spatial-temporal staging and unique anatomical detail of optic fissure closure (OFC) in the embryonic chick, including evidence for roles of apoptosis and epithelial remodelling. We performed complementary transcriptomic profiling and show that *Netrin*-1 (*NTN1*) is precisely expressed in the chick fissure margin at the fusion plate but is immediately downregulated after fusion. We further provide a combination of protein localisation and phenotypic evidence in chick, humans, mice and zebrafish that Netrin-1 has an evolutionarily conserved and essential requirement for OFC, and is likely to have an important role in palate fusion. Our data suggest that *NTN1* is a strong candidate locus for human coloboma and other multi-system developmental fusion defects, and show that chick OFC is a powerful model for epithelial fusion research.

INTRODUCTION.

Fusion of epithelia is an essential process during normal human development and its dysregulation can result in birth defects affecting the eye, heart, palate, neural tube, and multiple other tissues[1]. These can be highly disabling and are among the most common human birth defects, with prevalence as high as 1 in 500 [1–3]. Fusion in multiple embryonic contexts display both confounding differences and significant common mechanistic overlaps [1]. Most causative mutations have been identified in genes encoding transcription factors or signalling molecules that regulate the early events that guide initial patterning and outgrowth of epithelial tissues [1,3–5]. However, the true developmental basis of these disorders is more complex and a major challenge remains to fully understand the behaviours of epithelial cells directly involved in the fusion process.

Ocular coloboma (OC) is a structural eye defect that presents as missing tissue or a gap in the iris, ciliary body, choroid, retina and/or optic nerve. It arises from a failure of fusion at the optic fissure (OF; also referred to as the *choroid fissure*) in the ventral region of the embryonic eye cup early in development [4,6,7]. OC is the most common human congenital eye malformation and is a leading cause of childhood blindness that persists throughout life [2,8]. No treatments or preventative measures for coloboma are currently available.

The process of OF closure (OFC) requires the coordinated contributions of various cell types in the fusion environment along the anterior to posterior axis of the ventral eye cup (reviewed in [4,6]). In all vertebrates studied so far, these include epithelial cells of both the neural retina and retinal pigmented epithelium, and periocular mesenchymal (POM) cells of neural crest origin [4,9–12]. As the eye cup grows, the fissure margins come into apposition along the anterior-posterior axis and POM cells are gradually excluded. Through unknown mechanisms, the basal lamina that surround each opposing margin are either breached or dissolved and epithelial cells from each side intercalate and then subsequently reorganise to form a continuum of NR and RPE, complete with a continuous basal lamina. The function, requirement and behaviour of these epithelial cells in the fusing tissue, and their fates after fusion, are not well understood.

Some limited epidemiological evidence suggests environmental factors may contribute to coloboma incidence [7,13]. However, the disease is largely of genetic origin, with as many 39 monogenic OC-linked loci so far identified in humans and the existence of further candidates is strongly supported by evidence in gene-specific animal models [4]. Most known mutations cause syndromal coloboma, where the eye defect is associated with multiple systemic defects. A

common form of syndromal coloboma is CHARGE syndrome (MIM 214800) for which coloboma, choanal atresia, vestibular (inner-ear) and heart fusion defects are defining phenotypic criteria [14]. Palate fusion defects and orofacial-clefting are common additional features of CHARGE (~ 20% of cases) and in other monogenic syndromal colobomas (e.g. from deleterious mutations in *YAP1*, *MAB21L1*, and *TFAP2A* [15–17]), suggestive of common genetic mechanisms and aetiologies, and pleiotropic gene function.

Isolated (i.e. non-syndromal) OC may be associated with microphthalmia (small eye), and the majority of these cases are caused by mutations in a limited number of transcription-factor encoding genes that regulate early eye development (e.g. *PAX6*, *VSX2* and *MAF* [4,8]), implying that abnormal growth of the eye prevents correct OF margin apposition and that fusion defects are a secondary or an indirect phenotype. Indeed, none of these genes have yet been implicated with direct functional roles in epithelial fusion. However, many isolated coloboma cases also exist without microphthalmia, suggesting that in these patients, eye growth occurs normally but the fusion process itself is defective. These OCs are highly genetically heterogeneous and known loci are not recurrent among non-related patients [18]. Furthermore, despite large-scale sequencing projects, over 70% of all cases remain without a genetic cause identified [18].

The most effective and informative models for studying OFC so far have been mouse (*Mus musculus*) and zebrafish (*Danio rerio*). Both have significant experimental advantages, including powerful genetics and robust genomic data. In particular, live-cell imaging with fluorescent zebrafish embryos has proven to be useful in revealing some intricate cell behaviours at the fissure margin during fusion[12]. However, both models are restrictive for in depth molecular investigations due to their limited temporal windows of fusion progression and the number of cells actively mediating fusion and subsequent epithelial remodelling.

Here, we present accurate staging and anatomical detail of the process of chick OFC. We show the expansive developmental window of fusion, and the sizable fusion seam available for experimentation and analysis. We take advantage of this to perform transcriptional profiling at key discrete stages during fusion and show significant enrichment for known human OFC genes, and reveal multiple genes not previously associated with OFC. Our analyses also identified specific cellular behaviours at the fusion plate and found that apoptosis was a prominent feature during chick OFC. Furthermore, we reveal Netrin-1 as a mediator of OFC that is essential for normal eye development in evolutionarily diverse vertebrates, and which has a specific requirement during fusion in multiple developmental contexts. This study presents the chick as a

powerful model system for further OFC research, provides strong evidence for a novel candidate gene for ocular coloboma, and directly links epithelial fusion processes in the eye with those in broader embryonic tissues.

RESULTS.

OFC in the chick occurred within a wide spatial and temporal window.

The eye is the foremost observable feature in the chick embryo and grows exponentially through development (**Figure 1a**, **Figure 1—supplement 1**). The optic fissure margin (OFM) was first identifiable as a non-pigmented region at the ventral aspect of the eye that narrowed markedly in a temporal sequence as the eye increased in size (**Figure 1a**). To gain a clearer overview of gross fissure closure dynamics we first analysed a complete series of resected flat-mounted ventral eye tissue from accurately staged embryos at Hamburger Hamilton stages (HH.St) 25 through to HH.St34 (*n* >10 per stage; **Figure 1—supplement 1**). The OFM was positioned along the proximal-distal (P-D) axis of the eye, from the pupillary (or collar) region of the iris to the optic nerve. Progressive narrowing of the OFM was observed between HH.St27 to HH.St31, characterized by the appearance of fused OFM in the midline that separated the non-pigmented iris from the posterior OFM (**Figure 1—supplement 1**). Both these latter regions remained unpigmented throughout development and we found they were associated, respectively, with the development of the optic nerve and the pecten oculi - a homeostasis-mediating structure that extends out into the vitreous from the optic nerve head and is embedded in the posterior OFM (**Figure 1—supplement 1 & 2**) [19]. The anterior region of the pecten was attached to blood vessels that invade the eye globe through the open region of the iris OFM. This iris region remained open throughout development and well after hatching (**Figure 1—supplement 2**). A recent study reported that the posterior chick OFM closes via the intercalation of incoming astrocytes and the outgoing optic nerve[20], in a process that does not reflect the epithelial fusion processes seen during human optic fissure closure (e.g. mediated by epithelial cells of the RPE and neural retina)[9,20]. To assess the utility of the chick as a model for human OFC and epithelial fusion, we therefore focused our study on OFC progression in the distal and medial eye.

Using serial sections from memGFP[21] and wild-type embryos, we then unambiguously identified open fissure and fused seam regions of the medial-distal OFM (**Figure 1b**). The fused seams were defined by epithelial continuum in both the developing retinal pigmented epithelia

(RPE) and neural retina (NR) layers. We also identified the *fusion plates* undergoing fusion using sections and z-stack confocal microscopy (**Figure 1c**). Serial sectioning at stages HH.St25-34 provided qualitative data for the identification of fusion plates during the progression of chick OFC (**Table 1**). We then combined this data with fusion seam length measurements taken from flat mounted fissures to provide a robust quantitative framework of fusion progression (**Tables 2**). In all analyses, we observed no evidence for fusion in the medial or distal OFM at stages before HH.St27 (**Figure 1**; Figure 1**—supplement 1**; **Table 1**). Fusion was first initiated between HH.St27-28 as confirmed by the definitive appearance of joined epithelial margins at a single fusion point (FP). By HH.St29, the fused area had expanded to generate a fused seam of 0.56 mm (SD: ±0.12 mm; **Figure 1d-e**) with two fusion points, FP1 and FP2 at the distal and proximal limits, respectively. The position of FP1 became fixed at approximately 0.5 mm (SD: ±0.04 mm) from the developing pupillary region of the iris in all subsequent developmental stages (**Table 2**, *n* = 60 fissures analysed), and the region between FP1 and the iris remained fully open throughout ocular development (Figure 1**—supplement 2** and **Table 1**). In contrast, the location of FP2 became progressively more proximal until HH.St34 (**Table 2**), when FP2 was no longer distinguishable from the pecten (by flat mount or cryosections). This total expansion created a fused epithelial seam of ~1.7 mm at its maximum length (SD: ±0.07 mm, **Figure 1e**). In summary, we observed four distinct phases of fusion (**Figure 1f**): (1) *pre-fusion* when the entire OFM is open (up to HH.St27); (2) *fusion initiation* at HH.St27-28 in the medial OFM with the appearance of a single medial FP; (3) *active fusion* as two FPs separate with the expansion of a fused seam along the P-D axis (HH.St29-33); and (4) *complete fusion* as the entire OFM is fully fused in the medial OFM (by HH.St34). The process is active between HH.St27-HH.St34 and proceeds over ~66 hours.

Chick OFC was characterised by the breakdown of basement membranes, loss of epithelial morphology and localised apoptosis.

By defining fusion progression and the location of the fusion plates during chick OFC, we could then accurately assess the cellular environment within these regions. Immunostaining for the basement membrane (BM) basal lamina marker Laminin-B1 on cryo-sectioned fissure margins (**Figure 2a**) indicated that fusion occurs between cells of the RPE and neural retinal, as observed in human OFC[9]. Fusion between opposing margins was defined by a reduction of Laminin-B1 at the edges of the directly apposed fissures, followed the appearance of a

continuum of BM overlying the basal aspect of the neural retina. Periocular mesenchymal cells were removed from between the fissure margins as fusion progressed. Using a histological approach, we then provided evidence that both the RPE and NR directly contribute cells to the fusion plate (**Figure 2b**). We also observed that within the fusion plates there was marked epithelial remodelling of both cell types, beginning after apposition of the OFM edges. In contrast, at the fused seam we observed NR and RPE cells were realigned into apical-basal orientation and were indistinguishable from regions outside of the OFM, indicating that the fusion process was complete.

To determine whether the expanding seam between FP1 and FP2 was a result of active directional fusion (e.g. "zippering"), or was driven by localised cell-proliferation within the OFM seam (e.g. pushing forward static fusion plates), we used phospho-Histone-H3A (PH3A) as a marker for S-phase nuclei in mitotic cells and revealed there was no significant enrichment within the fusion seam (Figure 2**—supplement 1**). These results suggested that localised cell-proliferation within the seam was not a major mechanism for seam expansion during chick OFC, and further work is required to elucidate the precise mechanisms that drive seam expansion. We then sought to establish whether axonal ingression was a feature of chick OFC in the distal-medial OFM. Using Neurofilament-145 immunofluorescence, we found a complete absence of axonal processes in open, fusing, and fused regions of the distal-medial chick OFM (Figure 2**—supplement 2**). In contrast, at the same stages we found marked enrichment for axons within the proximal OFM and pecten region, providing further evidence that these regions of the chick optic fissure are distinct[20].

Programmed-cell death has been previously associated with epithelial fusion in multiple developmental contexts but the exact requirements for this process remain controversial [1]. Even within the same tissues differences arise between species - for example, apoptotic cells are clearly observed at the mouse fusion plate during OFC [10] but are not routinely found in zebrafish[12]. We therefore asked whether apoptosis was a major feature of chick OFC. Using HH.St30 eyes undergoing active fusion, we performed immunofluorescence staining for the pro-apoptotic marker activated Caspase-3. We consistently identified apoptotic foci within RPE and NR at both fusion plates, in the adjacent open fissure margin, and at the nascently fused seam with both cryo-section and whole-mount samples (**Figure 2c**; Figure 2**—supplement 2**). Foci were not found consistently in other regions of the eye or ventral retina (not shown). By quantifying the number of positive A-Casp-3 foci at FP2, we found that apoptosis was specifically

enriched in the active fusion environment but was absent from fused seam >120 µm and from open regions >250 µm beyond FP2 (**Figure 2d**), indicating that apoptosis is a specific feature of OFC in the chick eye.

Transcriptional profiling revealed genetic conservation between chick and human OFC.

We took advantage of the size and accessibility of the embryonic chick eye to perform transcriptomic profiling with the objectives of: (i) assessing the utility of the chick as a genetic model for human OFCD by expression for chick orthologues of known disease genes; and (ii) to identify novel genes that are required for optic fissure closure. Using HH.st25-26 eyes (pre-fusion; approx. embryonic day E5), segmental micro-dissection of the embryonic chick eye was first performed to obtain separate OFM, ventral eye, dorsal eye and whole eye samples (Figure 3—**Supplement 1**). We took care to not extract tissue from the pecten or optic nerve region of the developing OFM to ensure we obtained transcriptional data for the distal and medial OFM only. Cognate tissues were pooled, RNA was extracted, and region-specific transcriptomes were determined using total RNAseq and analysed to compare mean transcripts per million (TPM) values (**Figure 3-Source data 1**). Pseudoalignment to the Ensembl chicken transcriptome identified 30,265 expressed transcripts across all tissue types. To test whether this approach was sensitive enough to reveal domain-specific expression in the developing chick eye, we compared our RNAseq expression data for a panel of genes with clear regional specific expression from a previous study of mRNA *in situ* analyses in the early developing chick eye cup [22]. Markers of the early dorsal retina *(Efnb1, Efnb2, Vsx2, Tbx5, Aldh1A1*) clustered as dorsal-specific in our RNAseq data, whereas known ventral markers (*Crx, Maf1, Pax2, Aldh6(Ald1a3), Vax1, and Rax1*) were strongly expressed in our fissure and ventral transcriptomes (Figure 3—**Supplement 1**), which validated this approach to reveal OFC candidate genes.

We then repeated the analysis, collecting OFM, ventral tissue and whole eye and included stages HH.st27-28 (~E6; during initiation) and HH.st28-30 (~E7; during active fusion) as discrete time-points (Figure 3—**Supplement 1**). Dorsal tissue was not extracted for these stages. Correlation matrices for total transcriptomes of each sample indicated one of the HH.st25-26 fissure samples as an outlier, but otherwise there was close correlation between all the other samples (Pearson's correlation coefficient >0.9; Figure 3—**Supplement 1**). Quantitative analyses identified 14,262 upregulated genes and 14,125 downregulated genes in the fissure margin at the three time points (**Figure 3a**; fissure versus whole eye. False discovery rate (FDR) adjusted *p*-

value < 0.05). The largest proportion of these differential expressed genes (DEGs) were observed at HH.st25-27, most likely reflecting the periocular tissue between the fissure margins. Remarkably few DEGs were shared between stages. We used fold change (FC) analysis to identify biologically-relevant differential gene expression (Log_2FC ≥1.5 or ≤-1) in the fissure compared to whole eye, we found 1613, 2971 and 1491 DEGs at pre-fusion, initiation, and active fusion, respectively (**Figure 3-Source data 2**). Refining our analysis to identify only those DEGs common across all stages revealed 12 genes with increased expression in the fissure and 26 with decreased expression (**Figure 3b**; **Table 2**). Of these upregulated fissure-specific genes, causative mutations have previously been identified in orthologues of *PAX2*, *SMOC1*, *ALDH1A3*, and *VAX1* in human patients with coloboma or structural eye malformations [4,8], and some of these genes, such as PAX2 and inhibitors of BMP expression, induce coloboma phenotypes when overexpressed in the developing ventral chick eye[7,23]. In addition, targeted manipulations of orthologues of both *CHRDL1* and *CYP1B1* have recently been shown to cause coloboma phenotypes in *xenopus* and *zebrafish*, respectively [24,25]. The remaining fissure-specific genes (*NTN1*, *RTN4RL1*, *TFEC*, *GALNT6,* CLYBL and *RGMB*) had not been previously associated with OFC defects to the best of our knowledge.

Clustering analysis revealed *NTN1* as a fusion-specific OFC gene.

Clustering for relative expression levels of the RNAseq data at active fusion stages (HH.St28-30) revealed three independent clusters (2, 3, and 5) where expression profiles matched Fissure > ventral > whole eye (**Figure 3c**). We hypothesised that analysis of these clusters would reveal genes with fusion-specific functions during OFC. Of the three clusters with this profile, ontology analyses showed significant enrichment for sensory organ development and eye development processes (*FDR q*< 0.001, 10 genes) and for adhesion processes (Figure 3—**Supplement 1**; *FDR q*< 0.05, 25 genes; Biological adhesion [GO:0022610] and cell adhesion [GO:0022610]), of which 17 genes had mean TPM values >10. Within this group, multiple candidates for roles during OFC fusion were revealed, such as several transmembrane proteins, Integrin-A2, Cadherin-4, Collagen 18A1 and FLRT3 (**Figure 3d**). However, of these *NTN1* was the highest expressed and most fissure-specific (mean TPM values: Fissure = 204; ventral = 35; and whole eye = 4).

Netrin-1 was specifically and dynamically expressed in the fusing OFM.

We used RNAscope, colorimetric in situ hybridisation and immunostaining with NTN1-specific antibodies to determine the precise location of Netrin-1 in the chick eye (**Figure 4** and Figure 4—**Supplement 1**). We observed highly specific expression in both neuroepithelial retina and RPE cells at the fissure margins during active fusion at HH.St29-30 (**Figure 4a**). This was consistent to both fusion plates (FP1 and FP2), and in both locations *NTN1* expression was markedly reduced in the fused seam compared to expression in the adjacent open margins. Immunofluorescence revealed that, consistent with *NTN1* mRNA, NTN1 protein was specifically localised to the basal lamina at the opposing edges of the OFM, and to both RPE and neuroepithelial retina cells in this region (**Figure 4b-c**, Figure 4—**Supplement 1**). To test the significance of our findings to other vertebrates, we first asked whether this localisation was conserved to the human OFM. Immunofluorescence analysis for NTN1 (hNTN1) in human embryonic fissures during fusion stages (Carnegie Stage CS17) displayed remarkable overlap with our observations in chick, with protein signal localised specifically to open and fusion plate regions of OFM at the NR and RPE (**Figure 4d**), and an absence of hNTN1 in fused seam. Consistent with the protein localisation, RNAseq analysis on laser-captured human fissure tissue showed a 32x fold increase in *hNTN1* expression compared to dorsal eye (Patel and Sowden; *manuscript in preparation*). Microarray analyses had previously observed enrichment for *Ntn1* in the mouse fissure during closure stages[26], so we then analysed Ntn1 protein localisation in equivalent tissues in the mouse optic fissure (fusion occurs around embryonic day E11.5 and is mostly complete by E12.5[10]). We observed consistency in both cell-type and positional localisation of Ntn1 protein (**Figure 4e**), and that Ntn1 protein was not detected in the fused seam at E12.5 (immunoreactivity for NTN1 was observed in the proximal optic nerve region at this stage; Figure 4—**Supplement 2**).

Complete loss of Netrin caused coloboma and multisystem fusion defects in vertebrates.

Our results suggested that Netrin-1 has an evolutionarily conserved role in OFC and prompted us to test if NTN1 is essential for this process. We therefore analysed mouse embryos of WT and Netrin-null (*Ntn1*$^{-/-}$; Yung et al., 2015[27]) littermates at embryonic stages after OFC completion (E15.5-E16.5)[10] and observed highly penetrant ocular coloboma in *Ntn1*$^{-/-}$ mutants (> 90%; *n* = 10/11; **Figure 4f**). Mutant eyes analysed at earlier stages of eye development when fusion is first initiated [10] were normal (*n*=4 *Ntn1*$^{-/-}$ embryos; 8x eyes analysed in total), with fissure margins positioned directly in appositional contact each other (**Figure 4—Supplement 2**).

We also observed variably penetrant orofacial and palate fusion defects in mutant mice (**Figure 4g**; ~36%; n = 4/11 *Ntn1*$^{-/-}$ embryos), indicating that NTN1 may also have an important role in fusion during palatogenesis and craniofacial development.

Finally, we then tested whether Netrin deficiency would cause similar ocular defects in other vertebrates and generated germline *netrin*-1 mutant zebrafish by creating a nonsense mutation in the first exon of *ntn1a* using CRISPR/Cas9 gene editing (**Figure 4—Supplement 3**). We inter-crossed heterozygote G0 fish (*ntn1a*$^{+/-}$) and observed several G1 embryos displaying bilateral ocular defects including coloboma and microphthalmia (**Figure 4—Supplement 3**). DNA sequencing of the targeted *ntn1a* locus confirmed 100% (n=3) of the phenotypic embryos were homozygous, whereas ocular defects or colobomas were not observed in any heterozygous (n=6) or wild-type (n=12) embryos. A recent study applied morpholino (MO) translation-blocking knockdown approaches to target *ntn1a* in zebrafish embryos and observed bilateral ocular colobomas in all fish injectected[28], with normal early eye development and appropriately apposed fissure margins obvious prior to fusion. We were also able induce colobomas using MOs designed to target the translational start site of *ntn1a* (**Figure 4—Supplement 3**). Bilateral colobomas were observed in 31/71 (43.7%) of MO injected embryos with no ocular phenotypes observed in control injections (n=40). In combination, these results are in agreement with our data presented in chicken and mouse OFMs that Netrin-1 is essential for eye development and is likely to have a specific role in tissue fusion, and confirms an evolutionarily essential requirement for Netrin in ocular development, including OFC, in diverse vertebrate species.

DISCUSSION.

NTN1 is a strong candidate gene for coloboma and multisystem fusion defects.

Our study provides strong evidence that Netrin-1 is essential for optic fissure closure in the developing vertebrate eye and is required for normal orofacial development and palate fusion. The transient and specific *NTN1* expression at the fusion plate, and the subsequent reduction/loss in fused OFM, suggests NTN1 has a direct role in the fusion process. Indeed, Netrin1-deficient mouse eyes displayed highly penetrant colobomas but their fissure margins were normally apposed during fusion initiation, arguing against a broad failure of early eye development. In further support for a direct role in epithelial fusion was previously published work showing fusion failure during development of the vestibular system of both chick and mice where *NTN1*-expression was manipulated[27,29,30]. In this developmental context, otic epithelia must fuse normally for the correct formation of the semicircular canal structures. Although we and others[28] found coloboma in zebrafish knockdown experiments of *ntn1a*, we observed coloboma with microphthalmia in the context of complete knockout of *ntn1a*. This more severe phenotype in the complete absence of ntn1a implies there could be a more general requirement for Netrin-1 during early eye development, or could reflect teleost-specific eye developmental processes not shared among higher vertebrates[31]. Further work is required to elucidate the precise role of Netrin-1 during OFC and broader eye development among different species.

Taken in combination, these findings strongly implicate NTN1 as a multipotent factor required for tissue fusion in multiple distinct developmental contexts. In humans, variants near *NTN1* have been associated with cleft lip in human genome wide association studies[32,33]. While these are not monogenic disease mutations, this observation adds additional further relevance for future genetic studies of patients with coloboma. It is also consistent with our observations in *Netrin-1* knock-out animals having a high penetrance of both coloboma and cleft palate phenotypes. Therefore, we propose that *NTN1* should be included as a candidate gene in diagnostic sequencing of patients with human ocular coloboma, and should also be carefully considered for those with other congenital malformations involving defective fusion.

NTN1 may have a role in CHARGE syndrome.

Coloboma in association with additional fusion defects of the inner ear are two of the key clinical classifications for a diagnosis of CHARGE syndrome [14]. Further phenotypes commonly

associated with the syndrome are septal heart defects and orofacial clefting, both with aetiologies likely to involve fusion defects [1]. CHARGE syndrome cases are predominantly caused by heterozygous loss-of-function pathogenic variants in the chromodomain helicase DNA-binding protein 7 (*CHD7*) gene [34]. Mice lacking Chd7 display CHARGE syndrome-like phenotypes and exhibit abnormal expression of *Ntn1* [35,36]. In addition, ChIP-seq analyses have shown direct binding of Chd7 to the promoter region of *Ntn1* in mouse neural stem cells [37]. Given the amount of tissue available in the chick model, it would be possible and intriguing to confirm whether CHD7 directly regulates *NTN1* expression *in ovo* in the chick optic fissure. There is also emerging evidence that CHD7 and the vitamin A derivative retinoic acid (RA) indirectly interact at the genetic level during inner ear development [38]. Defective RA signalling also leads to significant reduction of *Ntn1* expression in the zebrafish OFM [39], implicating a possible genetic network involving RA and *CHD7,* where *NTN1* could directly mediate developmental fusion mechanisms from these hierarchical influences.

How does Netrin-1 mediate fusion?

Netrin-1 is well-studied for its canonical roles in guidance of commissural and peripheral motor axons and growth-cone dynamics, with attraction or repulsion mediated depending on the co-expression of specific receptors (reviewed in [40,41]). We found that axonal processes were absent from the chick fissure margin during fusion stages, suggesting that the normal function of NTN1 may be to prevent axon ingression into the OFM to permit fusion. However, the phenotypic evidence from both the palate and vestibular system strongly support the argument that NTN1 has a non-guidance mechanistic role during optic fissure closure. Netrin orthologues have been recently associated with cell migration and epithelial plasticity in the apparent absence of co-localised canonical receptors [42–44]. In contrast, netrin acting together with its receptor neogenin combined to mediate close adhesion of cell layers in the developing terminal end buds during lung branching morphogenesis [45]. Although we observed strong *NTN1* expression in cells lining the chick OFM, and similar localisation of Netrin-1 protein in chick, human and mouse, we did not observe reciprocal expression of any canonical NTN1 receptors in our RNAseq datasets (e.g. UNC5, DCC or Neogenin; Figure 2—**Supplement 4**). Indeed, the Netrin repulsive cue *UNC5B* was the most significantly downregulated DEG in fissure versus whole eye in our data and was downregulated in human OFM (Sowden & Patel; *manuscript in preparation*). Therefore, it will be vitally important for future studies to elucidate interaction partners of

Netrin in fusing tissues, or to reveal if Nerin-1 can act autonomously in these contexts to provide deeper insight into its mechanistic function during fusion.

The chick is a powerful model for OFC.

The chick is one of the oldest models for developmental biology and has provided many key insights into human developmental processes [46]. Despite this, and extensive historical study of eye development in chicken embryos, the process of chick optic fissure closure has not been well analysed until now. Indeed, the first study appeared only recently and specifically defined aspects of tissue fusion at the proximal (optic nerve and pecten) region of the OF[20], and did not observe complete fusion of epithelia in these regions. Indeed, closure of the proximal OF was characterised by intercalation of pecten and the lack of true epithelial continuum of neuroepithelial retina and RPE. By focusing on the epithelial fusion events in the distal and medial eye, our study complements the Bernstein et al study[20] to provide a comprehensive framework of OFC progression in the chick. Indeed, our analyses clearly define three distinct and separate anatomical regions in the developing chick OFM: the iris, the medial OFM, and the pecten. We present the spatial and temporal sequence of chick OFC at the anatomical and molecular level, and provide strict criteria for staging the process - based on a combination of broad embryonic anatomy, ocular, and fissure-specific features. Fusion initiated at the medial OFM at HH.St27/28 and continued until HH.St34, with predominantly distal to proximal directionality. In addition, we found that closure of the medial OFM is a true epithelial fusion process that occurs over a large time window of approximately 60 hours, involving two fusion plates, and that closes over 1.5 mm of complete fusion seam. This temporal window, the number of directly contributing cells, and the accurate staging of its progression allows unique opportunities for further experimentation. Importantly, one whole chick optic fissure (from HH.St29 onwards) can simultaneously provide data for unfused, fusing, and post-fused contexts.

In addition, our transcriptional profiling, including the identification of OFM-specific genes in the chick that include multiple human coloboma orthologues, builds on previous work that illustrate the chick as an excellent model for human eye development and the basis of embryonic malformations[19,47,48]. These features, in combination with recent advances in chick transgenics and genetic manipulations[49], project the chick as a powerful to analyse cell behaviours during OFC and epithelial fusion. For example, the stable multi-fluorescent Cre-inducible lineage tracing line (the Chameleon chicken [49]) will be valuable to determine how the

fissure-lining cells contribute to the fusing epithelia, while the very-recent development of introducing gene-targeted or gene-edited primordial germ cells into sterile hosts for germ-line transmission [50] provides a rapid and cost-effective way to develop stable genetic lines to interrogate specific gene function [49,51]. Thus, our study illustrates the powerful utility of the chick as a model for investigating OFC and for the discovery of novel candidate genes for coloboma, and is perfectly timed to coincide with major new developmental biology techniques in avian systems to place the chick model as a powerful addition to OFC and fusion research.

Summary.

This study provides the first detailed report of epithelial fusion during chick optic fissure closure and illustrates the power of the embryonic chick eye to investigate the mechanisms guiding this important developmental process further and to provide insights into human eye development and broader fusion contexts. We clearly define the temporal framework for OFC progression and reveal that fusion is characterised by loss of epithelial cell types and a marked coincidental increase in apoptosis. We reveal the specific expression of orthologues of known coloboma-associated genes during chick OFC, and provide a broad transcriptomic dataset that can improve the identification of candidate genes from human patient exome and whole-genome DNA sequencing datasets. Finally, we identify that *NTN1* is specifically and dynamically expressed in the fusing vertebrate fissure - consistent with having a direct role in epithelial fusion, and is essential for OFC and palate development. *NTN1* should therefore now be considered as a new candidate for ocular coloboma and congenital malformations that feature defective epithelial tissue fusion.

MATERIALS AND METHODS

Key resources table

Reagent type (species) or resource	Designation	Source or reference	Identifiers	Additional information
genetic reagent (M. musculus)	Ntn1-/-	PMID 26395479	MGI:5888900	Lisa Goodrich (Harvard Medical School, Boston MA).
biological sample (G. gallus)	memGFP	PMID 25812521	Rozbicki 2015	Maintained at The Greenwood Building, Roslin Institute, UK.
biological sample (Gallus gallus)	Chicken eye and OFM dissections	This paper	Hy-Line Brown	Maintained at The Greenwood Building, Roslin Institute, UK.
antibody	NTN1 (Mouse monoclonal)	R&D Systems	MAB128	1 in 100 dilution for whole mount IF
antibody	NTN1 (Rabbit polyclonal)	abcam	ab126729	1 in 300 dilution for human and mouse IF; 1 in 500 dilution for chick cryosection IF
antibody	Laminin-B1 (Mouse monoclonal)	DSHB	3H11	1 in 20 dilution for all IF
antibody	NF145 (Rabbit polyclonal)	Merk	AB1987	1 in 100 dilution for all IF
antibody	Phospho-Histone H3A (Rabbit monoclonal)	Cell Signalling Technologies	#3377	1 in 200 for cryosections, 1 in 1000 for flat-mount
antibody	Activated Caspase-3 (Rabbit polyclonal)	BD Pharminagen	#559565	1 in 400 dilution for all IF
commercial assay or kit	Alexa Fluor Phalloidin (488 nm)	Thermo-Fisher	#A12379	1 in 40 dilution for all IF
software, algorithm	Kallisto	PMID 27043002	NA	NA
software, algorithm	Limma	PMID 25605792	NA	NA

Embryo processing. Hy-Line Eggs were incubated at 37^{o}C at day 0 (E0), with embryo collection as stated throughout the text. Whole embryos were staged according to Hamburger Hamilton [52,53]. Heads were removed and either ventral eye tissue was resected and flat-mounted and imaged

immediately, or whole heads were placed in ice cold 4 % paraformaldehyde (PFA) in pH 7.0 phosphate buffered saline (PBS), overnight and then rinsed twice in PBS. OFMs used for fusion progression measurements (flat mounts) were mounted in Hydromount (National Diagnostics HS-106) between a coverslip and glass slide, without fixation. Whole embryo, flat mounted OFMs, and dissected eye images for were captured on a Leica MZ8 light microscope and measurements were processed using FIJI (NCBI/NIH open source software [54]).

Immunofluorescence. For cryosections, resected ventral chick eyes were equilibrated in 15% Sucrose-PBS then placed at 37°C in 7% gelatin:15% Sucrose, embedded and flash-frozen in isopentane at -80°C. Sections were cut at 20 µm. Immunofluorescence was performed on chick fissure sections as follows: 2x 30 min rinse in PBS, followed by 2 hours blocking in 1 % BSA (Sigma) in PBS with 0.1 % Triton-X-100 [IF Buffer 1]. Sections were incubated overnight at 4°C with primary antibodies diluted in 0.1 % BSA in PBS with 0.1 % Triton-X-100 [IF Buffer 2]. Slides were then washed in 3x 20 min PBS, followed by incubation for 1 hour with secondary antibodies (Alexa Fluor conjugated with 488nm or 594 nm fluorophores; 1:800-1000 dilution, Thermo Fisher), and mounted with ProLong Antifade Gold (Thermo Fisher) with DAPI. Alexa Fluor Phalloidin (488 nm; Thermo-Fisher #A12379) was added at the secondary antibody incubation stages (1:50 dilution). Human foetal eyes were obtained from the Joint Medical Research Council UK (grant # G0700089)/Wellcome Trust (grant # GR082557) Human Developmental Biology Resource (http://www.hdbr.org/). For Netrin-1 immunostaining in human and mouse tissues, cryosections were antigen retrieved using 10 mM Sodium Citrate Buffer, pH 6.0 and blocked in 10 % Goat serum+ 0.2 % Triton-X100 in PBS, then incubated overnight at 4°C with primary antibody (Abcam #ab126729; 1: 300) in block. Secondary antibody staining and subsequent processing were the same as for chick. For whole-mount immunofluorescence we followed the protocol from Ahnfelt-Rønne et al [55], with the exception that we omitted the TNB stages and incubated instead with IF Buffer 1 (see above) overnight and then in IF Buffer 2 for subsequent antibody incubation stages, each for 24 h at 4 °C. No signal amplification was used. Antibodies were used against Phospho-Histone H3A and Netrin-1. Imaging was performed using a Leica DM-LB epifluorescence microscope, or a Nikon C1 inverted confocal microscope and Nikon EZ-C1 Elements (version 3.90 Gold) software. All downstream analysis was performed using FIJI. Image analysis for proliferation in the OFM on flat-mounts was performed by counting Phospho-Histone H3A positive foci using a region of interest grid

with fixed dimensions of 200 µm^2 and throughout the entire confocal Z-stack. To quantitate apoptotic foci at the OFM, we used Activated-Casp3 immunofluorescence on serial cryosections of HH.St29-30 OFMs and collected confocal images for each section along the P-D axis. Image analysis was performed by counting A-Casp3 positive foci at the OFM in sequential sections using a region of interest with fixed dimensions of 100 µm^2. For histology and subsequent haematoxylin and eosin staining, resected eyes processed and image captured according to Trejo-Reveles et al [48].

In situ hybridization. RNAscope was performed on HH.St29 cryosections using a probe designed specific to chicken *NTN1* according to Nishitani et al [30]. For colourimetric in situ hybridisation, a ribprobe was for *NTN1* was designed using PCR primers to amplify a 500 bp product from cDNA prepared from chick whole embryos at HH.St28-32 (Oligonucleotide primers: Fwd 5'-ATTAACCCTCACTAAAGGCTGCAAGGAGGGCTTCTACC-3' and Rev 5'-TAATACGACTCACTATAGGCACCAGGCTGCTCTTGTCC-3'). The PCR products were purified and transcribed into DIG-labelled RNA using T7 polymerase (Sigma-Aldrich) and used for In Situ hybridization on cryosectioned chick fissure margin tissue (prepared as described above for immunofluorescence) or whole embryos using standard protocols (described in J. Rainger's doctoral thesis - available on request).

Transgenic animal work. To obtain *Ntn1*$^{-/-}$ mouse embryos (Ntn1$^{tm1.1Good}$, RRID:MGI:5888900), we performed timed matings with male and female heterozygotes and took the appearance of a vaginal plug in the morning to indicate embryonic day (E)0.5. Embryos were collected at E11.5 and E16.6 and genotyped according to Yung et al[27]. As with this previous report we observed ratios within the expected range for all three expected genotypes (28 total embryos: 13x *Ntn1*$^{+/-}$; 10x *Ntn1*$^{-/-}$; 5x WT – 46%; 35%; 18%, respectively). Embryos were fixed in 4 % paraformaldehyde overnight and then rinsed in PBS and imaged using a Leica MZ8 light microscope. *Ntn1*$^{-/-}$ and C57Bl/6J animals were maintained on a standard 12-hour light-dark cycle. Mice received food and water ad lib and were provided with fresh bedding and nesting daily. For zebrafish work, we designed gene-editing sgRNA oligos alleles to target *ntn1a*: 5´-GGTCTGACGCGTCGCACGTG-3´. We then generated founder (G0) animals by zygotic microinjection of CRISPR/Cas9 components according to previous work [56–58]. G0 animals were genotyped and used for crosses to generate G1 embryos which were scored for coloboma phenotypes and genotyped individually (Figure 4—

514 **Supplement 3**). All experiments were conducted in agreement with the Animals (Scientific
515 Procedures) Act 1986 and the Association for Research in Vision and Ophthalmology Statement
516 for the Use of Animals in Ophthalmic and Vision Research (USA). Morpholinos were designed
517 and generated by Gene Tools LLC (Oregon) to target the translation initiating site of *ntn1a*: 5'-
518 CATCAGAGACTCTCAACATCCTCGC-3', and a Universal control MO sequence was used as a
519 control: 5'-ATCCAGGAGGCAGTTCGCTCATCTG-3'. One cell stage embryos were injected with 2.5
520 ng or 5.0 ng of ntn1a or control morpholino and allowed to develop to OFC stages (≥48hpf).
521 Oligos used for *ntn1a* genotyping by sanger sequencing were: 5'-TTACGACGAGAACGGACACC-3'
522 and 5'-GGAGGTAATTGTCCGACTGC-3'.
523
524 **Transcriptional profiling.** For RNA seq analysis, we carefully dissected regions of (i) fissure-
525 margin, (ii) ventral eye, and (iii) dorsal eye, and (iv) whole eye tissue from ≥10 individual
526 embryos for each HH stage range (Figure 3—**Supplement 1**). Samples were collected and pooled
527 for each tissue type and stage to obtain *n*=3 technical replicate RNA pools per tissue type per
528 stage. Total RNA was extracted using Trizol (Thermo Scientific). Whole-transcriptome cDNA
529 libraries were then prepared for each pool following initial mRNA enrichment using the Ion RNA-
530 Seq Core Kit v2, Ion Xpress RNA-Seq Barcodes, and the Ion RNA-Seq Primer Set v2 (Thermo
531 Scientific). cDNA quality was confirmed using an Agilent 2100 Bioanalyzer. Libraries were pooled,
532 diluted, and templates were prepared for sequencing on the Ion Proton System using Ion PI
533 chips (Thermo Scientific). Quantitative transcriptomics was performed using Kallisto
534 psuedoalignment [59] to the Ensembl (release 89) chicken transcriptome. Kallisto transcript counts
535 were imported into R using tximport[60] and differentially expressed transcripts identified using
536 Limma [61] . Genes not expressed in at least three samples were excluded. To identify the
537 relationships between samples, Log2 transformed counts per million were then calculated using
538 edgeR [62] and Spearman's rank correlation was used to identify the similarities in genome-wide
539 expression levels between samples. All RNAseq data files are submitted to the NCBI Gene
540 Expression Omnibus database (http://www.ncbi.nlm.nih.gov/geo) with the accession number
541 GSE84916.
542
543 **Statistical analysis.** Bar graphs display means ± SD or 95% confidence intervals as indicated.
544 Sample sizes were n≥3, unless stated otherwise. Statistical analyses were performed using Prism
545 8 (GraphPad Software Inc.). Data was assessed for normal distribution by Shapiro-Wilk test

where appropriate. Significance was evaluated by unpaired Student's t-test, where $p \leq 0.05$ was deemed significant. Asterisk indicate significance in Figure 1 as *p ≤ 0.05. **p ≤ 0.01, ***p ≤ 0.001.

ACKNOWLEDGEMENTS

We wish to thank Megan Davey at Roslin Institute for academic discussions and support, David FitzPatrick at The MRC IGMM for supporting the RNAseq pilot experiments, Jenny Chen at NIE for technical assistance with zebrafish transgenics, Sadie Schlabach at HMS for help with embryo genotyping and sample collection, Richard Clark at The WTCRF in Edinburgh, and Agnes Gallagher at MRC IGMM for RNA-sequencing.

COMPETING INTERESTS

No financial or non-financial competing interests are declared for all authors.

REFERENCES

1. Ray, H. J. & Niswander, L. Mechanisms of tissue fusion during development. *Development* **139**, 1701–1711 (2012).
2. Morrison, D. *et al.* National study of microphthalmia, anophthalmia, and coloboma (MAC) in Scotland: investigation of genetic aetiology. *J. Med. Genet.* **39**, 16–22 (2002).
3. Nikolopoulou, E., Galea, G. L., Rolo, A., Greene, N. D. E. & Copp, A. J. Neural tube closure: cellular, molecular and biomechanical mechanisms. *Development* **144**, 552–566 (2017).
4. Patel, A. & Sowden, J. C. Genes and pathways in optic fissure closure. *Semin. Cell Dev. Biol.* (2017). doi:10.1016/j.semcdb.2017.10.010
5. Kohli, S. S. & Kohli, V. S. A comprehensive review of the genetic basis of cleft lip and palate. *J Oral Maxillofac Pathol* **16**, 64–72 (2012).
6. Onwochei, B. C., Simon, J. W., Bateman, J. B., Couture, K. C. & Mir, E. Ocular Colobomata. *Survey of Ophthalmology* **45**, 175–194 (2000).
7. Gregory-Evans, C. Y., Williams, M. J., Halford, S. & Gregory-Evans, K. Ocular coloboma: a reassessment in the age of molecular neuroscience. *J. Med. Genet.* **41**, 881–91 (2004).
8. Williamson, K. A. & FitzPatrick, D. R. The genetic architecture of microphthalmia, anophthalmia and coloboma. *Eur. J. Med. Genet.* **57**, 369–380 (2014).
9. O'Rahilly R. The early development of the eye in staged human embryos. *Carnegie instn Wash Publ* **625**, 1–42 (1966).
10. Hero, I. Optic fissure closure in the normal cinnamon mouse: An ultrastructural study. *Investig. Ophthalmol. Vis. Sci.* **31**, 197–216 (1990).
11. Hero, I. The optic fissure in the normal and microphthalmic mouse. *Exp. Eye Res.* **49**, 229–239 (1989).
12. Gestri, G., Bazin-Lopez, N., Scholes, C. & Wilson, S. W. Cell Behaviors during Closure of the Choroid Fissure in the Developing Eye. *Front. Cell. Neurosci.* **12**, 1–12 (2018).
13. Hornby, S. J., Ward, S. J. & Gilbert, C. E. Eye birth defects in humans may be caused by a recessively-inherited genetic predisposition to the effects of maternal vitamin A deficiency during pregnancy. *Med Sci Monit* **9**, HY23-6 (2003).
14. Verloes, A. Updated diagnostic criteria for CHARGE syndrome: A proposal. *American Journal of Medical Genetics* (2005). doi:10.1002/ajmg.a.30559
15. Rainger, J. *et al.* Monoallelic and biallelic mutations in MAB21L2 cause a spectrum of major eye malformations. *Am. J. Hum. Genet.* **94**, 915–923 (2014).
16. Williamson, K. A. *et al.* Heterozygous loss-of-function mutations in YAP1 cause both isolated and syndromic optic fissure closure defects. *Am. J. Hum. Genet.* **94**, 295–302 (2014).
17. Doherty, R. & Lea, D. Branchio-oculo-facial and branchio-oto-renal syndromes are distinct entities. *Clinical Genetics* (1992). doi:10.1111/j.1399-0004.1992.tb03667.x
18. Rainger, J. *et al.* A recurrent de novo mutation in ACTG1 causes isolated ocular coloboma. *Hum. Mutat.* **38**, 942–946 (2017).
19. Wisely, C. E. *et al.* The chick eye in vision research: An excellent model for the study of ocular disease. *Prog. Retin. Eye Res.* **61**, 72–97 (2017).
20. Bernstein, C. S. *et al.* The cellular bases of choroid fissure formation and closure. *Dev. Biol.* **440**, 137–151 (2018).
21. Rozbicki, E. *et al.* Myosin-II-mediated cell shape changes and cell intercalation contribute to primitive streak formation. *Nat. Cell Biol.* (2015). doi:10.1038/ncb3138
22. Peters, M. a & Cepko, C. L. The dorsal-ventral axis of the neural retina is divided into multiple domains of restricted gene expression which exhibit features of lineage

compartments. *Dev. Biol.* **251**, 59–73 (2002).
23. Sehgal, R., Karcavich, R., Carlson, S. & Belecky-Adams, T. L. Ectopic Pax2 expression in chick ventral optic cup phenocopies loss of Pax2 expression. *Dev. Biol.* **319**, 23–33 (2008).
24. Pfirrmann, T. *et al.* Molecular mechanism of CHRDL1-mediated X-linked megalocornea in humans and in Xenopus model. *Hum. Mol. Genet.* **24**, 3119–3132 (2014).
25. Williams, A. L., Eason, J., Chawla, B. & Bohnsack, B. L. Cyp1b1 regulates ocular fissure closure through a retinoic acid–independent pathway. *Investig. Ophthalmol. Vis. Sci.* **58**, 1084–1097 (2017).
26. Brown, J. D. *et al.* Expression profiling during ocular development identifies 2 Nlz genes with a critical role in optic fissure closure. *Proc. Natl. Acad. Sci. U. S. A.* **106**, 1462–7 (2009).
27. Yung, A. R., Nishitani, A. M. & Goodrich, L. V. Phenotypic analysis of mice completely lacking Netrin-1. *Development* 3686–3691 (2015). doi:10.1242/dev.128942
28. Richardson, R. *et al.* Transcriptome profiling of zebrafish optic fissure fusion. *Sci. Rep.* **9**, 1–12 (2019).
29. Salminen, M., Meyer, B. I., Bober, E. & Gruss, P. Netrin 1 is required for semicircular canal formation in the mouse inner ear. *Development* **127**, 13–22 (2000).
30. Nishitani, A. M. *et al.* Distinct functions for netrin 1 in chicken and murine semicircular canal morphogenesis. *Development* **144**, 3349–3360 (2017).
31. Martinez-Morales, J. R., Cavodeassi, F. & Bovolenta, P. Coordinated morphogenetic mechanisms shape the vertebrate eye. *Front. Neurosci.* **11**, 1–8 (2017).
32. Leslie, E. J. *et al.* A multi-ethnic genome-wide association study identifies novel loci for non-syndromic cleft lip with or without cleft palate on 2p 24.2, 17q23 and 19q13. *Hum. Mol. Genet.* (2016). doi:10.1093/hmg/ddw104
33. Leslie, E. J. *et al.* Identification of functional variants for cleft lip with or without cleft palate in or near PAX7, FGFR2, and NOG by targeted sequencing of GWAS loci. *Am. J. Hum. Genet.* (2015). doi:10.1016/j.ajhg.2015.01.004
34. Vissers, L. E. L. M. *et al.* Mutations in a new member of the chromodomain gene family cause CHARGE syndrome. *Nat. Genet.* (2004). doi:10.1038/ng1407
35. Hurd, E. A. *et al.* Loss of Chd7 function in gene-trapped reporter mice is embryonic lethal and associated with severe defects in multiple developing tissues. *Mamm. Genome* **18**, 94–104 (2007).
36. Hurd, E. A., Micucci, J. A., Reamer, E. N. & Martin, D. M. Delayed fusion and altered gene expression contribute to semicircular canal defects in Chd7 deficient mice. *Mech. Dev.* (2012). doi:10.1016/j.mod.2012.06.002
37. Engelen, E. *et al.* Sox2 cooperates with Chd7 to regulate genes that are mutated in human syndromes. *Nat. Genet.* (2011). doi:10.1038/ng.825
38. Yao, H. *et al.* CHD7 represses the retinoic acid synthesis enzyme ALDH1A3 during inner ear development. *JCI Insight* **3**, 1–19 (2018).
39. Lupo, G. *et al.* Retinoic acid receptor signaling regulates choroid fissure closure through independent mechanisms in the ventral optic cup and periocular mesenchyme. *Proc. Natl. Acad. Sci. U. S. A.* **108**, 8698–8703 (2011).
40. Lai Wing Sun, K., Correia, J. P. & Kennedy, T. E. Netrins: versatile extracellular cues with diverse functions. *Development* **138**, 2153–69 (2011).
41. Larrieu-Lahargue, F., Thomas, K. R. & Li, D. Y. Netrin Ligands and Receptors: Lessons From Neurons to the Endothelium. *Trends Cardiovasc. Med.* **22**, 44–47 (2012).
42. Manhire-Heath, R., Golenkina, S., Saint, R. & Murray, M. J. Netrin-dependent

downregulation of Frazzled/DCC is required for the dissociation of the peripodial epithelium in Drosophila. *Nat. Commun.* **4**, 1–10 (2013).
43. Lee, S.-J. *et al.* Netrin-1 Induces MMP-12-Dependent E-Cadherin Degradation Via the Distinct Activation of PKCα and FAK/Fyn in Promoting Mesenchymal Stem Cell Motility. *Stem Cells Dev.* **23**, 1870–1882 (2014).
44. Yan, W. *et al.* Netrin-1 induces epithelial-mesenchymal transition and promotes hepatocellular carcinoma invasiveness. *Dig. Dis. Sci.* **59**, 1213–1221 (2014).
45. Srinivasan, K., Strickland, P., Valdes, A., Shin, G. C. & Hinck, L. Netrin-1/neogenin interaction stabilizes multipotent progenitor cap cells during mammary gland morphogenesis. *Dev. Cell* **4**, 371–382 (2003).
46. Stern, C. The chick model system: A distinguished past and a great future. *International Journal of Developmental Biology* (2018). doi:10.1387/ijdb.170270cs
47. Vergara, M. N. & Canto-Soler, M. V. Rediscovering the chick embryo as a model to study retinal development. *Neural Dev.* **7**, 22–40 (2012).
48. Trejo-Reveles, V., McTeir, L., Summers, K. & Rainger, J. An analysis of anterior segment development in the chicken eye. *Mech. Dev.* **150**, (2018).
49. Davey, M. G., Balic, A., Rainger, J., Sang, H. M. & McGrew, M. J. Illuminating the chicken model through genetic modification. *Int. J. Dev. Biol.* (2018).
50. Taylor, L. *et al.* Efficient TALEN-mediated gene targeting of chicken primordial germ cells. *Development* **144**, 928–934 (2017).
51. Woodcock, M. E., Idoko-Akoh, A. & McGrew, M. J. Gene editing in birds takes flight. *Mamm. Genome* **28**, 1–9 (2017).
52. Hamburger, V. & Hamilton, H. L. A series of normal stages in the development of the chick embryo. 1951. *Dev. Dyn.* **195**, 231–272 (1992).
53. Hamburger, V. & Hamilton, H. L. A series of normal stages in the development of the chick embryo. *J. Morphol.* **88**, 49–92 (1951).
54. Schindelin, J. *et al.* Fiji: An open-source platform for biological-image analysis. *Nature Methods* **9**, 676–682 (2012).
55. Ahnfelt-Ronne, J. *et al.* An Improved Method for 3D Reconstruction of Protein Expression Patterns in Intact Mouse and Chicken Embryos and Organs. *J Histochem Cytochem* (2007).
56. Dutta, S. *et al.* Nlz1 is required for cilia formation in zebrafish embryogenesis. *Dev. Biol.* (2015). doi:10.1016/j.ydbio.2015.08.019
57. Varshney, G. K. *et al.* High-throughput gene targeting and phenotyping in zebrafish using CRISPR/Cas9. *Genome Res.* (2015). doi:10.1101/gr.186379.114
58. Jao, L.-E., Wente, S. R. & Chen, W. Efficient multiplex biallelic zebrafish genome editing using a CRISPR nuclease system. *Proc. Natl. Acad. Sci.* (2013). doi:10.1073/pnas.1308335110
59. Bray, N. L., Pimentel, H., Melsted, P. & Pachter, L. Near-optimal probabilistic RNA-seq quantification. *Nat. Biotechnol.* **34**, 525–7 (2016).
60. Soneson, C., Love, M. I. & Robinson, M. D. Differential analyses for RNA-seq: transcript-level estimates improve gene-level inferences. *F1000Research* (2016). doi:10.12688/f1000research.7563.2
61. Ritchie, M. E. *et al.* Limma powers differential expression analyses for RNA-sequencing and microarray studies. *Nucleic Acids Res.* (2015). doi:10.1093/nar/gkv007
62. Robinson, M. D., McCarthy, D. J. & Smyth, G. K. edgeR: A Bioconductor package for differential expression analysis of digital gene expression data. *Bioinformatics* (2009). doi:10.1093/bioinformatics/btp616

63. Cho, S.-H. & Cepko, C. L. Wnt2b/beta-catenin-mediated canonical Wnt signaling determines the peripheral fates of the chick eye. *Development* **133**, 3167–3177 (2006).

TABLES.

	Fusion plates identified		
HH Stage	**1x FP only**	**Both FP1 & FP2**	***n* per stage**
25	0	0	4
26	0	0	4
27	1	0	3
28	3	1	4
29	1	4	5
30	0	4	4
31	0	3	3
32	0	5	5
33	1	2	3
34	3	0	3

Table 1. Qualitative analysis of fusion plates observed per developmental stage by cryosections and H&E.

HH Stage	Mean total OFM length (mm)	± SD	Mean length of fused seam (mm)	± SD
27	2.20	0.15	-	-
28	2.92	0.33	*	*
29	3.58	0.28	0.56	0.12
30	4.38	0.17	0.93	0.09
31	4.50	0.25	1.09	0.13
32	4.77	0.16	1.15	0.10
33	5.31	0.23	1.39	0.10
34	5.67	0.16	1.70	0.07

Table 2. Quantitative measurements of key features during OFC progression using flat mounted WT and mem-GFP fissures. Total OFM length includes optic nerve and pecten. * Any fused fissures observed were too small to measure (<0.1 mm).

ENSEMBL ID	HGNC ID	LogFC: Fissure Vs Whole (HH.St25-27) ~E5	FDR Adjusted *p* value	LogFC: Fissure Vs Whole (HH.St27-28) ~E6	FDR Adjusted *p* value	LogFC: Fissure Vs Whole (HH.St28-30) ~E7	FDR Adjusted *p* value
ENSGALG00000023626	*NTN1*	3.98	5.11E-05	4.34	8.16E-05	5.41	3.06E-07
ENSGALG00000005689	*PAX2*	3.48	9.36E-06	3.41	2.11E-05	3.18	4.14E-06
ENSGALG00000033365	*ALDH6*	2.97	1.00E-05	3.94	1.75E-04	3.00	4.91E-05
ENSGALG00000016875	*novel gene*	2.21	4.57E-05	3.56	8.72E-07	3.55	2.62E-08
ENSGALG00000009415	*SMOC1*	3.49	1.46E-05	2.36	3.92E-03	2.60	8.93E-05
ENSGALG00000025822	*CYP1B1*	2.95	1.11E-05	2.03	1.34E-02	3.02	1.55E-05
ENSGALG00000021589	*RTN4RL1*	2.41	5.79E-03	2.43	8.00E-03	2.69	4.22E-04
ENSGALG00000040557	*TFEC*	1.93	8.70E-03	2.35	5.01E-03	2.90	9.86E-04
ENSGALG00000009261	*VAX1*	1.99	6.95E-04	1.96	3.15E-03	2.49	1.55E-05
ENSGALG00000041101	*GALNT6*	1.78	3.45E-04	2.07	6.97E-04	2.55	6.85E-06
ENSGALG00000008072	*CHRDL1*	1.79	3.85E-05	1.86	1.03E-03	1.94	2.49E-05
ENSGALG00000015284	*RGMB*	1.89	1.37E-02	1.73	2.43E-02	1.76	7.63E-03
ENSGALG00000011413	*novel gene*	-1.53	1.13E-02	-1.34	3.34E-02	-1.69	1.60E-02
ENSGALG00000004270	*ALDH1A2*	-1.20	4.06E-02	-1.80	9.46E-03	-1.76	2.74E-03
ENSGALG00000010801	*TMEM61*	-2.07	8.63E-03	-1.49	3.77E-02	-1.93	5.90E-03
ENSGALG00000003842	*GHRH*	-1.33	4.58E-02	-2.60	1.48E-02	-2.62	5.28E-03
ENSGALG00000012712	*RBM24*	-2.57	9.39E-04	-2.00	1.69E-02	-2.35	2.80E-03
ENSGALG00000012644	*novel gene*	-1.85	4.91E-03	-2.58	1.38E-02	-3.18	9.33E-04
ENSGALG00000003324	*PRRX1*	-1.52	4.65E-02	-2.77	2.21E-02	-3.42	1.32E-03
ENSGALG00000007706	*FGF8*	-2.20	2.94E-03	-3.10	8.72E-04	-2.64	9.86E-04
ENSGALG00000010929	*SPARCL1*	-3.16	3.03E-03	-1.77	4.19E-02	-3.17	6.48E-04
ENSGALG00000034585	*CP49*	-3.65	6.32E-06	-1.93	1.55E-02	-2.59	3.60E-04
ENSGALG00000038848	*MSX2*	-2.19	4.15E-03	-3.35	1.15E-02	-2.92	5.01E-03
ENSGALG00000004279	*GRIFIN*	-3.97	7.94E-04	-2.71	2.55E-02	-1.92	4.89E-02
ENSGALG00000004569	*UNC5B*	-1.41	4.81E-03	-4.14	4.56E-08	-3.21	2.62E-08
ENSGALG00000019802	*novel gene*	-2.24	1.56E-02	-3.43	4.36E-02	-3.59	9.52E-03
ENSGALG00000043175	*novel gene*	-3.59	7.36E-03	-2.99	3.27E-02	-2.91	2.59E-02
ENSGALG00000005613	*novel gene*	-2.96	6.50E-04	-2.21	1.99E-02	-4.40	2.06E-04
ENSGALG00000015015	*CYTL1*	-2.43	3.39E-02	-3.13	4.74E-02	-5.14	5.01E-03
ENSGALG00000004035	*CRYBA1*	-5.04	1.21E-04	-2.56	1.95E-02	-3.33	2.00E-03
ENSGALG00000006189	*CRYGN*	-4.66	6.22E-04	-4.25	1.82E-02	-4.97	9.33E-04
ENSGALG00000012470	*LYPD6*	-2.49	1.20E-02	-4.64	6.97E-04	-7.13	5.09E-06
ENSGALG00000008253	*TBX5*	-3.50	3.48E-04	-6.73	5.98E-04	-4.39	6.02E-05
ENSGALG00000015147	*ALDH1A1*	-5.06	1.46E-05	-4.96	1.22E-04	-4.79	1.55E-05
ENSGALG00000042119	*MIP*	-4.47	2.10E-03	-5.43	3.97E-02	-6.15	3.54E-03
ENSGALG00000005634	*CRYBA4*	-5.47	2.65E-04	-4.94	1.61E-02	-7.17	6.56E-04
ENSGALG00000005630	*CRYBB1*	-5.36	1.72E-04	-6.97	4.56E-03	-6.24	1.37E-04
ENSGALG00000008735	*BFSP1*	-6.48	5.53E-04	-6.23	1.76E-02	-8.63	1.97E-03

Table 3. Fissure Specific Differentially expressed genes (q< 0.05; LogFC: ≥1.5 and ≤-1) at all stages analysed. Genes with increased expression are depicted in grey.

FIGURE LEGENDS.

Figure 1. Analysis of chick optic fissure closure. (***a***) Chicken embryos at HH.St25 and HH.St30 illustrated the optic fissure (OF; arrows) as a non-pigmented region in the ventral aspect of the developing eye. (***b***) *Left*: Schematic showing orientation of the developing chick optic fissure with respect to the embryonic whole eye. Dorsal-ventral and Proximal-distal axes are indicated. This study focused on the medial optic fissure (marked by white hatching) distal to the developing pecten and optic nerve. *Right*: brightfield and fluorescent confocal microscopy using memGFP cryosections illustrated the open (arrow) and fused seam (arrowhead) regions in chick OFM. The location and planes of the cut sections along the D-P axis are indicated in the accompanying schematic. (***c***) Brightfield and fluorescent confocal microscopy of memGFP OFM sections unambiguously defined the location of fusion plates (arrowheads, top and middle panels) at all stages throughout OFC, combined with flat-mounted memGFPs. Bottom panel: representative single plane confocal image clearly indicated FP2. (***d***) Brightfield microscopy of flat-mounted ventral eyes revealed the tissue dynamics during closure and coinciding with location of fusion plates (FPs). At HH.St29 the medial OFM had narrowed markedly along the P-D axis between the iris and the proximal region, with FP1 and FP2 (arrowheads) closely positioned in the distal OF. At HH.St31 the medial OFM had become fully pigmented in the fused seam, and the distance between FP1 and FP2 (arrowheads) had lengthened in the P-D axis. An opening remained in the OFM at the iris region (asterisk). (***e***) Histogram to illustrate fused seam length at each HH stage (error bars = 1x s.d.). Quantitative data of OFM progression obtained from flat mounts and cryosections is provided in Table 1. (***f***) Schematic representation of chick OFC progression in the distal and medial retina. *1. Pre-fusion*: A fully open OFM is evident in the ventral retina at stages HH.St25-27; *2. Initiation*: At HH.St27-28 the first fused region is observed in the distal-medial OFM; *3. Active fusion*: fusion extends briefly in the distal direction but then stops in the presumptive iris to leave an open region throughout development. Fusion proceeds markedly proximally with FP2 extending towards the pecten. *4. Complete fusion*: Fusion stops proximally when FP2 meets the fused pecten region. The fusion seam is complete with a complete continuum of both NR and RPE layers in the ventral eye. Abbreviations: L, lens; OC, optic cup, OF, optic fissure; ON, optic nerve; FP, fusion plate; HH, Hamburger Hamilton staging; RPE, retinal pigmented epithelia; NR, neural retina; POM, periocular mesenchyme.

Figure 2. Basement membrane remodelling, loss of epithelial characteristics and apoptosis are defining features of Chick OFC. (***a***) Immunostaining for the basement membrane (BM) component Laminin-B1 and nuclear staining (DAPI) using confocal microscopy illustrated that fusion was preceded by the dissolution of BM (compare arrowheads in boxes) as the fissure margins came into contact at the fusion plate, and that fusion was characterised by the generation of a BM continuum at the basal aspect of the neural retina (arrows). Nuclear staining indicated that cells of the retinal pigmented epithelium (RPE) and neural retina (NR) contributed to the fusion plate and that periocular mesenchymal cells were removed from the region between the apposed margins. Images are from a single OFM and are representative of $n \geq 3$ samples. (***b***) H&E staining on paraffin sections at FP2 showed apposed fissure margins with well organised epithelia in NR and RPE (-40 µm from FP2); subsequent sections at the fusion plate showed loss of epithelial organisation in both cell types (within hatching); at the fused seam (+ 200 µm from FP2) continuous organised layers were observed in both NR and RPE epithelia. Note that fusion occurred from contributions of both NR and RPE. (***c***) Immunostaining for the apoptosis marker activated Caspase-3 (A-Casp3) on serial cryo-sectioned OFMs (HH.St30) using

confocal microscopy (average image projections) indicated that A-Casp3 positive foci (arrows) were enriched in epithelia at the OFM and in the nascently fused seam. The midline OFM, including the fusion points, is indicated by yellow arrowheads in all panels. OFMs were counterstained with DAPI. ***(d)*** Quantitation of A-Casp3 foci from serially-sectioned OFMs confirmed significant enrichment at FP2, with a graded reduction in apoptotic cells in both directions away from the fusion plate. Data shown is the mean of all measurements (*n* =4); error bars = 95% Confidence intervals. Scale bars = 25 µm in ***a*** and ***c***, = 20 µm in ***b***.

Figure 3. Transcriptional profiling in chick optic fissure closure. (***a***) Transcriptional profiling using microdissected regions of the developing chick eye at E5 (HH.St25-27; pre-fusion), E6 (HH.St27-28; initiation), and E7 (HH.St28-30; during active fusion) revealed multiple DEGs at each stage. (***b***) *NTN1* was the highest expressing gene of 12 fissure-specific DEGs (fissure vs whole eye) throughout all stages of chick OFC (Log2 FC >1.5; FDR < 0.05). These included the known human coloboma associated genes (indicated by #): *SMOC1*, *PAX2, VAX1* and *ALDH6,* in addition to the coloboma candidates from other animal studies *CHRDL1* and *CYP1B1* (indicated by •). (***c***) Clustering for relative expression levels at active fusion stages (HH.St28-30) revealed three independent clusters (2, 3, and 5) where expression levels trended with Fissure > ventral > whole eye. (***d***) Analysis of normalised mean expression values (TPM, n=3 technical replicates; error bars = 1x standard deviation) from clusters 2, 3, 5 at HH.St28-30 for the Gene Ontology enriched pathways (*p*< 0.0001; Biological fusion [GO:0022610], and Epithelial fusion [GO:0022610]) revealed significant fissure-specific expression for highly expressed (TPM> 100) genes - *NTN1*, *FLRT3*, *CYP1B1* and *COL18A1* - in addition to other potential candidate genes for roles in OFC. *NTN1* (TPM> 200) was the highest expressed fissure-specific DEG identified during active fusion.

Figure 4. A conserved fusion-specific requirement for NTN1 in OFC and palate development. (***a***) RNAscope analysis of *NTN1* mRNA (green, and grey in insets) in HH.St29 OFMs revealed fissure-specific *NTN1* expression (arrows) with strongest signal observed at open regions and in the fusion plate, and reduced expression in the adjacently fused seam. *NTN1* expression was localised to cells of both the NR and RPE. Fusion progression was indicated using anti-laminin co-immunofluorescence (magenta). Images shown are maximum intensity projections of confocal Z-stacks. (***b***) Single-plane confocal images of immunofluorescence analysis for NTN1 on flat-mounted distal (FP1) and proximal (FP2) OFM revealed enriched protein localisation at the edges of the open fissure margins and reduced in the fused seam. (***c***) Immunostaining on cryosectioned OFM at the open and fusion plate at HH.St29 revealed NTN1 was specifically localised to the basal lamina (arrowheads) and to the epithelia of the neural retina and RPE (arrows) at the OFM. (***d***) Immunostaining on CS17 human foetal eye sections revealed human Netrin-1 (hNTN1) was localised to NR epithelia (arrows) and at the overlying basal lamina (dented arrowheads) at the fissure margins. hNTN1 was absent from the fused seam epithelia. (***e***) Immunostaining for mouse Netrin-1 (mNtn1) in during active fusion stages (E11.5) showed mNtn1 was localised at the open fissure margins (arrow) in the basal lamina and to cells at the NR-RPE junction. mNtn1 was absent from this region in fused OFM seam at E12.5. (***f***) *Ntn1*$^{-/-}$ mice exhibited highly penetrant (~90 %) bilateral coloboma (*arrows; n* = 10/11 homozygous E15.5-E16.5 animals analysed). (***g***) Cleft secondary palate (arrows) was observed in ~ 36 % of *Ntn1*$^{-/-}$ embryos at E15.5-E16.5 (4/11 homozygous animals).

SUPPORTING INFORMATION

Figure 3-Source data 1

Kallisto analysis of RNAseq data from segmentally dissected HH.St25-26/E5 chick eyes.

Figure 3-Source data 2

Limma analysis of RNAseq data from segmentally dissected chick eyes at all stages.

SUPPLEMENTAL FIGURES AND LEGENDS.

Figure 1: Supplement-1. (**a**) Mean eye diameter measurements for chick at embryonic days E4-E8 ($n \geq 5$ eyes per stage). (**b**) Representative images of whole embryos and corresponding flat-mounted fissures from fusion-relevant Hamburger Hamilton[52,53] embryonic stages. The approximate point of the initiating fusion plate is indicated for a HH.St28 fissure (white arrow). A minimum of 3 fissures were examined by confocal light-microscopy to identify fusion points and then additional samples were processed by serial cryo-sectioning to confirm fusion plates and fused seams. (**c**) Whole embryo (*Top panels*) and memGPF confocal Z-stack images (*Lower panels*) at HH.St25 and HH.St26 positioned at the distal and medial OFM in the P-D axis illustrated lack of fusion at the iris and fissure margin. (**d**) Representative H&E sections from fissures at HH.St25 and HH.St26 confirming lack of fusion at these stages. Note the abutted OFM but un-fused (arrow) at the iris region in HH.St25 OFM (*enlarged panel*). Panel labels i-iii correspond to positions indicated in ***c***.

Figure 1: Supplement-2. (**a**) Iris development in flat mounted OFMs from E8-E10. Note the OFM at the iris remains open and is non-pigmented throughout all stages analysed (arrowheads). (**b**) Location and orientation of the developing pecten oculi and associated blood vessel (arrows) entering at the open iris region (arrowheads) shown in eyes taken from embryos at E9-19. The pecten was partially dissected from the underlying tissue (asterisks) to indicate its location relevant to the proximal optic fissure (yellow hatching). The P-D axes are shown.

Figure 2: Supplement-1. (**a**) Schema for quantifying Phospho-Histone H3A foci within confocal Z-stacks taken of whole mounted fissures using a region of interest grid system. (**b**) Representative image showing positive nuclei (red). ROI grids used were 200 x 200 μm; all positive foci were recorded. P-D axis is shown for **a** & **b**. (**c**) Quantified Phospho-Histone H3A immunostaining of whole-mounted fissures. Fewer proliferating cells (p=0.1093) were observed at HH.St29 within the seam (mean=66.0, SD=20.30) compared to outside the seam (mean=90.8, SD=32.6), and at HH.St30 (p=0.0063; mean fused seam =86.8, SD=32.3; within seam mean=60.2, SD=21.8); Student's t-test used to compare within and outside seam. Data shown is the mean of three fissures per stage with standard deviations indicated. *Note:* Central seam length was too small to quantify in HH.St29 fissures (< 200 μm), however phospho-Histone H3A foci were fewer at the fusion points compared to non-seam regions. (**d**) Representative phospho-Histone H3A immunostaining of serially-sectioned fissures at HH.St29 revealed the presence of mitotic cells within the apical neural retina throughout the ventral eye. Phospho-Histone H3A was not enriched in the fused seam (HH.St30; n=3).

Figure 2: Supplement-2. (**a**) Anti-Neurofilament immunostaining (NF145, Neurofilament medium; *Top panels*) in the OFM during active fusion. NF145 immunoreactivity (green) was absent from the distal and medial OFM but was observed in the proximal region at the developing pecten and optic nerve. Immunostaining on sections (*middle panels*) taken at the fused seam, the apposed OFM, and at the central retina confirmed the absence of axons in epithelial tissues at the open OFM and the nascently-fused OFM. Panel labels correspond to positions indicated in the HH.St30 flat-mount brightfield image (*Bottom*). (***b***) *Top:* Combined bright-field and fluorescence confocal imaging (Z-stack projections) of whole mount anti-activated Caspase-3 immunostaining in a HH.St30 fissure showed positive foci in the fused seam at a ~100 μm from the static FP1, and multiple positive foci within the fused seam >100 μm FP2.

Below: Enlarged images of FP1 and FP2 from (***b***) counterstained with DAPI highlighted the enrichment for A-Casp3 foci at FP2 (open margin is indicated by hatching).

Figure 3: Supplement-1 (**a**) Schema for segmental microdissection of OFM samples prior to RNA extraction and processing for RNAseq. At least 10 fissures from independent chick embryos were used per sample, per stage. Care was taken to exclude capture of the proximal/pecten OFM region. Lenses were included for whole eye samples, for which 4 whole-eyes from independent embryos were used. (**b**) Heat map for E5 (HH.St25-27) RNAseq data shows strict domain specificity for genes with previously known spatial restriction [63]. (***c***) Heatmap showing a correlation coefficient of >0.9 (Spearman's rank correlation) for genome-wide expression levels for all RNAseq samples. Note that sample Fiss_E5_3 is an outlier. (**d**) GOrilla Gene Ontology analysis for upregulated DEGs at all-stages using "Processes" revealed significant enrichment for five processes. Number of genes in intersection is given in brackets, FDR q values are given for each ontology. GO terms and descriptions: GO:0007423, sensory organ development; GO:0001654, eye development; GO:0007155, cell adhesion; GO:0022610, biological adhesion, GO:0051239, regulation of multicellular organismal process.

Figure 4: Supplement-1 (**a**) Whole-mount *in situ* hybridisation revealed *NTN1* expression in the ventral eye, developing pharyngeal arches, and otic vesicles at HH.St22. Enlarged panels showed regionally-restricted *NTN1* expression in the developing fissure margins (arrows) at HH.St22 (*Top*) and HH.St24 (*Bottom*). (**b**) Section in situ hybridisation and NTN1 immunofluorescence analyses at HH.St28 showed *NTN1* expression was specific to the edges of the early medial OFM immediately prior to fusion. (**c**) (*Top panels*) RNAscope analyses at FP1/distal OFM at HH.St29 showed *NTN1* mRNA specificity (arrows) in the fissure margin and a graded reduction in the fused seam. (*Bottom*) Positive control analyses for RNAscope showed strong *NTN1* mRNA signals in the basal floorplate of the neural tube at HH.St29. The OFM midline is shown by a yellow arrowhead in all panels.

Figure 4: Supplement-2 (**a**) Immunofluorescence staining for mouse Ntn1 in wild-type E12.5 eyes post-fusion showed absence of Ntn1 signal (arrowheads) in the distal (A) and medially fused OFM (B), but presence of Ntn1 (arrowheads) in the proximal (C) and optic disc (D) regions. (**b**) E11.5 *Ntn1*$^{-/-}$ embryos did not show any obvious size or gross structural differences during active fusion stages (*n*=4 *Ntn1*$^{-/-}$ embryos analysed, total = 8 eyes). Ventral tissue at the optic fissures (OF, arrows) appeared to be normally apposed. (**c**) Sections from Wild-type and *Ntn1*$^{-/-}$ optic fissures immmunostained with anti-laminin antibody (green) and counterstained with DAPI and Phalloidin (red) showed mutant OFMs aligned correctly at E11.5 with no clear structural differences observed between the genotypes. Representative sections from distal, medial, and proximal OFMs are shown. OF, optic fissure; NR, neural retina; RPE, retinal pigmented epithelium.

Figure 4: Supplement-3 (**a**) Gene-editing strategy using a single sgRNA targeting the first exon of zebrafish *ntn1a*. CRISPR/Cas9 was used to generate heterozygous (*ntn1*$^{+/-}$; G0) founders. These were crossed to generate homozygous G1 embryos (*ntn1*$^{-/-}$). (**b**)) Panels showing the coloboma microphthalmia and coloboma (arrow) phenotypes in gene-edited *ntn1*$^{-/-}$ embryos compared to wild-type. (**c**) Sanger sequencing confirmed the homozygous gene-edited *ntn1a* allele in 100% of phenotypic G1 embryos. (**d**) In silico translation of encoded mutant allele aligned to wild-type (first 153 amino acids shown of 603 aa ntn1a protein are shown). The gene edited mutation

encodes a frame-shift in the first exon resulting in a truncated ntn1a of 105 amino acids (p.Cys90Ala.fs15). (**e**) Morpholino experiments produced bilateral coloboma in 100% of embryos injected with *ntn1a* translation-blocking MO, with no ocular phenotypes observed in control MO injected embryos. The optic fissures are indicated by arrows. (**f**) Tables with penetrance of colobomas in gene-edited embryos and MO embryos compared to controls.

Figure 4: Supplement-4 Analysis of TPM values from RNAseq data at all three stages did not detect significant levels of expression for canonical NTN1 receptors in the ventral eye or fissures during OFC stages. *ITGB1* showed the highest expression values throughout all stages, but was not specific to the fissure margin or ventral eye tissues.

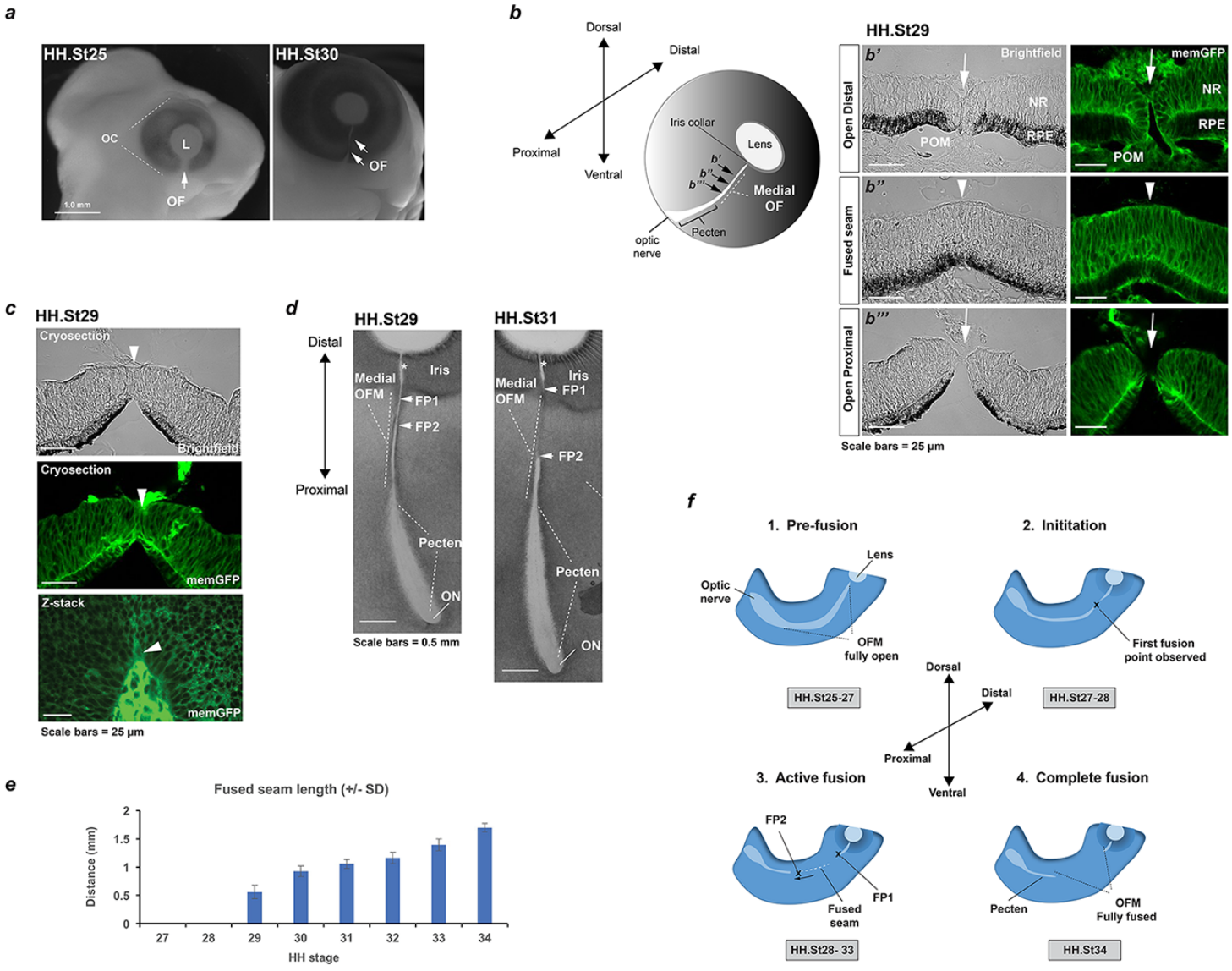
a
HH.St25
HH.St30
OC
L
OF
OF
1.0 mm
b
Dorsal
Distal
Proximal
Ventral
Iris collar
Lens
b'
b''
b'''
Medial
OF
optic
nerve
Pecten
HH.St29
Open Distal
Fused seam
Open Proximal
b'
Brightfield
NR
RPE
POM
memGFP
NR
RPE
POM
b''
b'''
Scale bars = 25 µm
c
HH.St29
Cryosection
Brightfield
Cryosection
memGFP
Z-stack
memGFP
Scale bars = 25 µm
d
Distal
Proximal
HH.St29
Medial
OFM
Iris
FP1
FP2
Pecten
ON
Scale bars = 0.5 mm
HH.St31
Medial
OFM
Iris
FP1
FP2
Pecten
ON
e
Fused seam length (+/- SD)
Distance (mm)
2
1.5
1
0.5
0
27
28
29
30
31
32
33
34
HH stage
f
1. Pre-fusion
Lens
Optic
nerve
OFM
fully open
HH.St25-27
2. Inititation
First fusion
point observed
HH.St27-28
Dorsal
Distal
Proximal
Ventral
3. Active fusion
FP2
FP1
Fused
seam
HH.St28- 33
4. Complete fusion
Pecten
OFM
Fully fused
HH.St34

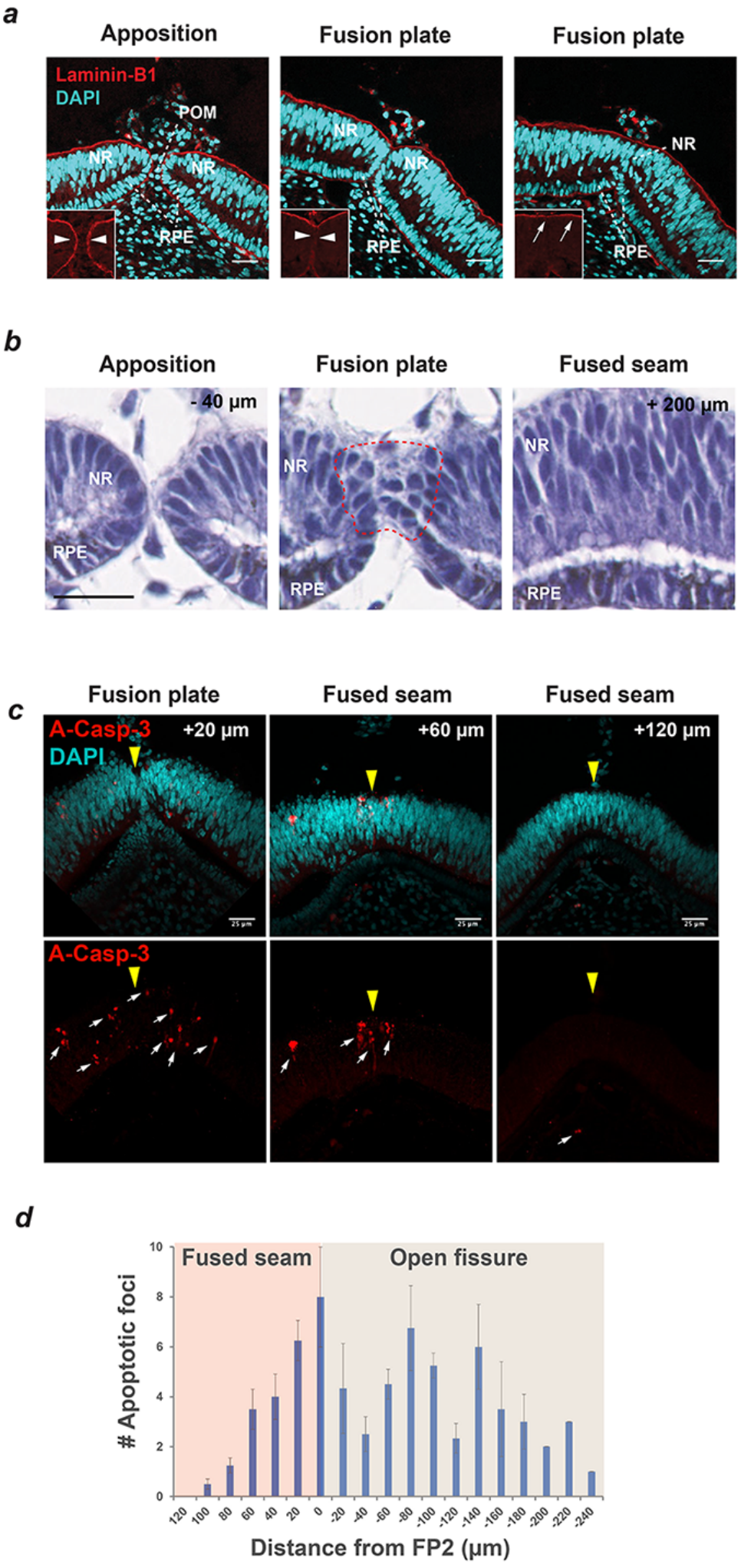
a
Apposition
Fusion plate
Fusion plate
Laminin-B1
DAPI
POM
NR
NR
RPE
NR
NR
RPE
NR
RPE
b
Apposition
Fusion plate
Fused seam
- 40 µm
NR
RPE
NR
RPE
+ 200 µm
NR
RPE
c
Fusion plate
Fused seam
Fused seam
A-Casp-3
DAPI
+20 µm
+60 µm
+120 µm
A-Casp-3
d
Fused seam
Open fissure
Apoptotic foci
Distance from FP2 (µm)

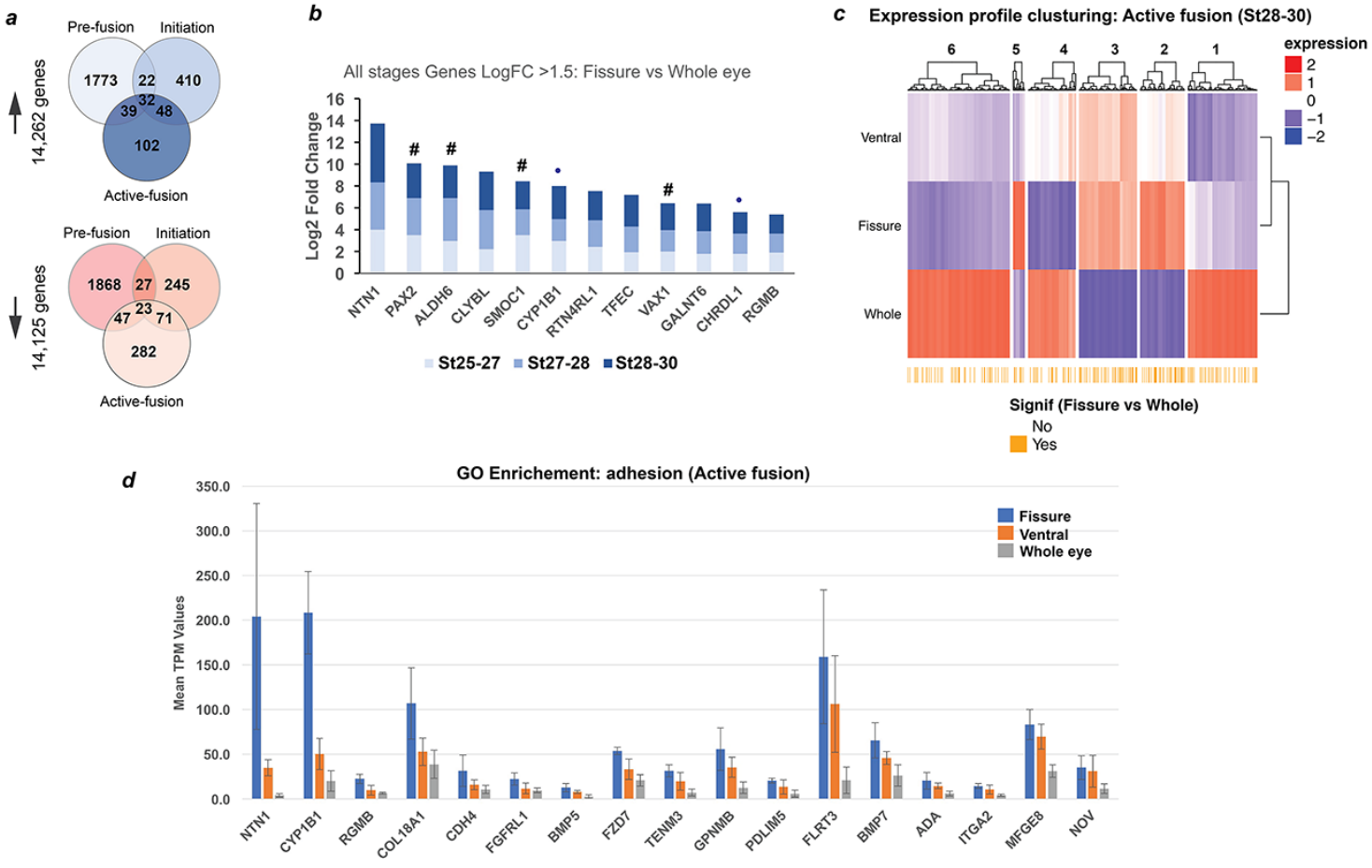
a
Pre-fusion
Initiation
1773
22
410
32
39
48
102
Active-fusion
14,262 genes
Pre-fusion
Initiation
1868
27
245
23
47
71
282
Active-fusion
14,125 genes
b
All stages Genes LogFC >1.5: Fissure vs Whole eye
Log2 Fold Change
NTN1
PAX2
ALDH6
CLYBL
SMOC1
CYP1B1
RTN4RL1
TFEC
VAX1
GALNT6
CHRDL1
RGMB
St25-27
St27-28
St28-30
c
Expression profile clusturing: Active fusion (St28-30)
6
5
4
3
2
1
expression
Ventral
Fissure
Whole
Signif (Fissure vs Whole)
No
Yes
d
GO Enrichement: adhesion (Active fusion)
Mean TPM Values
Fissure
Ventral
Whole eye
NTN1
CYP1B1
RGMB
COL18A1
CDH4
FGFRL1
BMP5
FZD7
TENM3
GPNMB
PDLIM5
FLRT3
BMP7
ADA
ITGA2
MFGE8
NOV

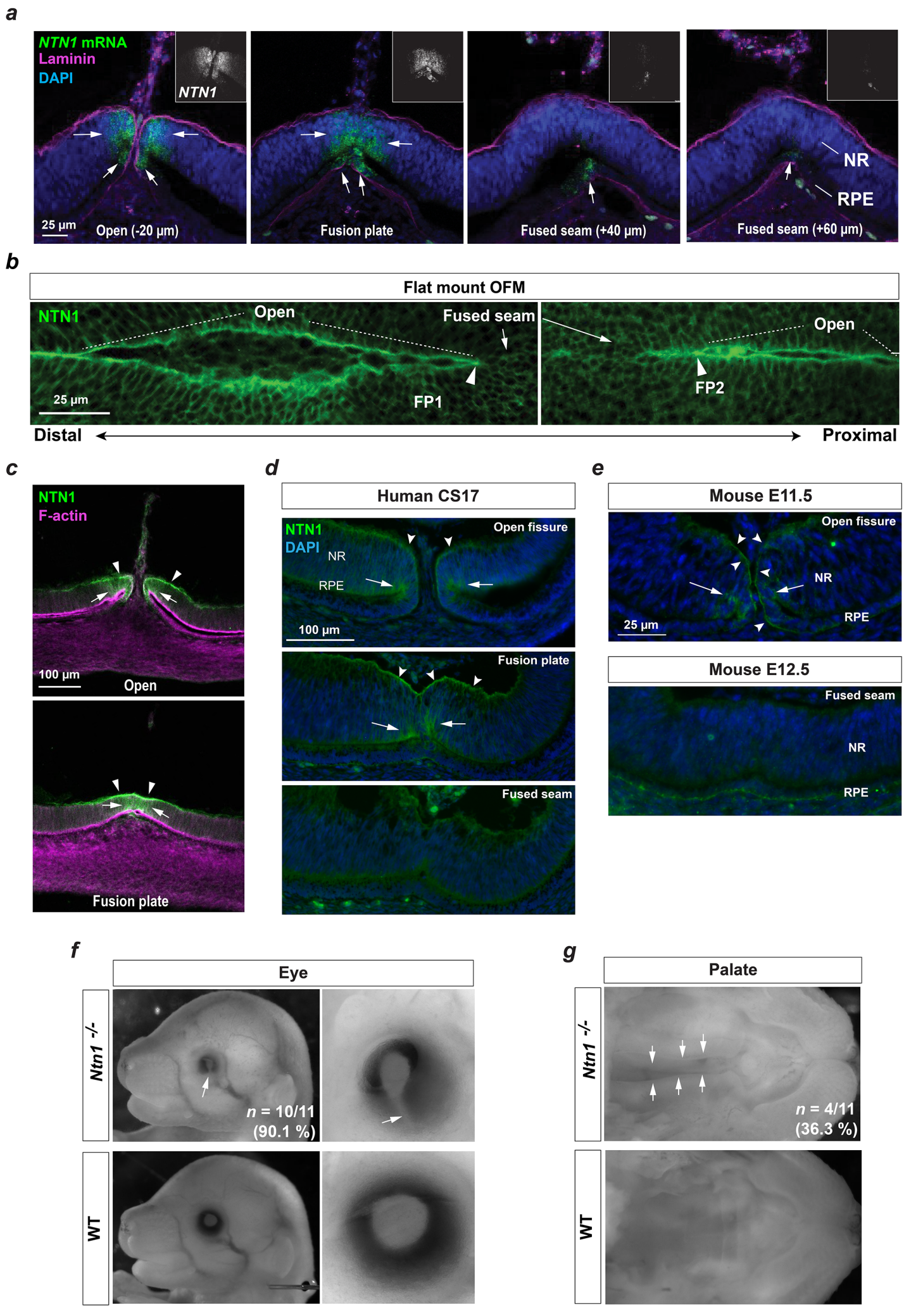
a
NTN1 mRNA
Laminin
DAPI
NTN1
25 µm
Open (-20 µm)
Fusion plate
Fused seam (+40 µm)
NR
RPE
Fused seam (+60 µm)
b
Flat mount OFM
NTN1
Open
Fused seam
25 µm
FP1
Open
FP2
Distal
Proximal
c
NTN1
F-actin
100 µm
Open
Fusion plate
d
Human CS17
NTN1
DAPI
NR
RPE
Open fissure
100 µm
Fusion plate
Fused seam
e
Mouse E11.5
Open fissure
NR
RPE
25 µm
Mouse E12.5
Fused seam
NR
RPE
f
Eye
Ntn1 -/-
n = 10/11
(90.1 %)
WT
g
Palate
Ntn1 -/-
n = 4/11
(36.3 %)
WT

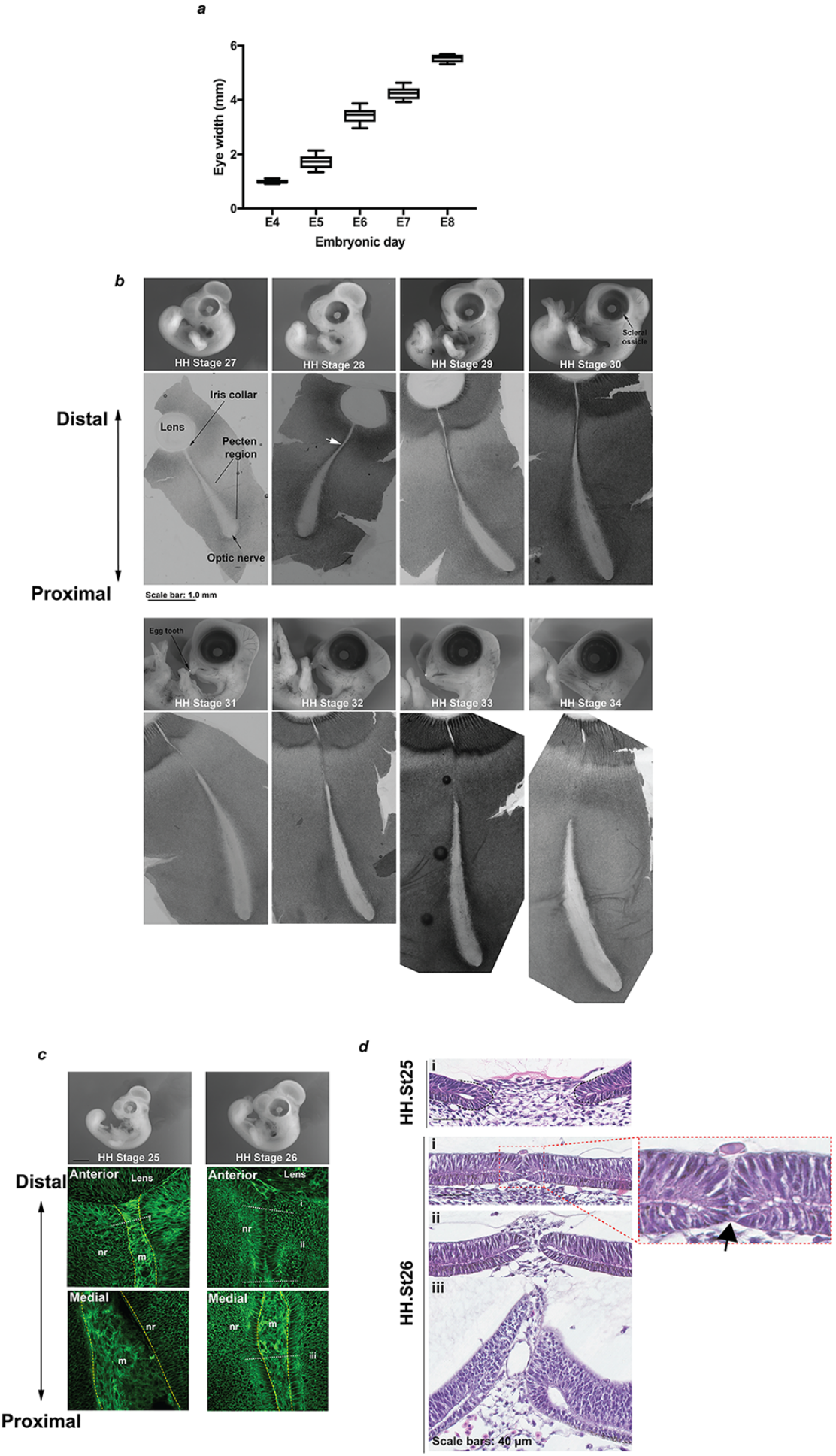
a
Eye width (mm)
0
2
4
6
E4
E5
E6
E7
E8
Embryonic day
b
HH Stage 27
HH Stage 28
HH Stage 29
HH Stage 30
Scleral ossicle
Iris collar
Lens
Pecten region
Optic nerve
Distal
Proximal
Scale bar: 1.0 mm
Egg tooth
HH Stage 31
HH Stage 32
HH Stage 33
HH Stage 34
c
HH Stage 25
HH Stage 26
Distal
Anterior
Lens
nr
m
Medial
i
ii
iii
Proximal
d
HH.St25
HH.St26
Scale bars: 40 µm

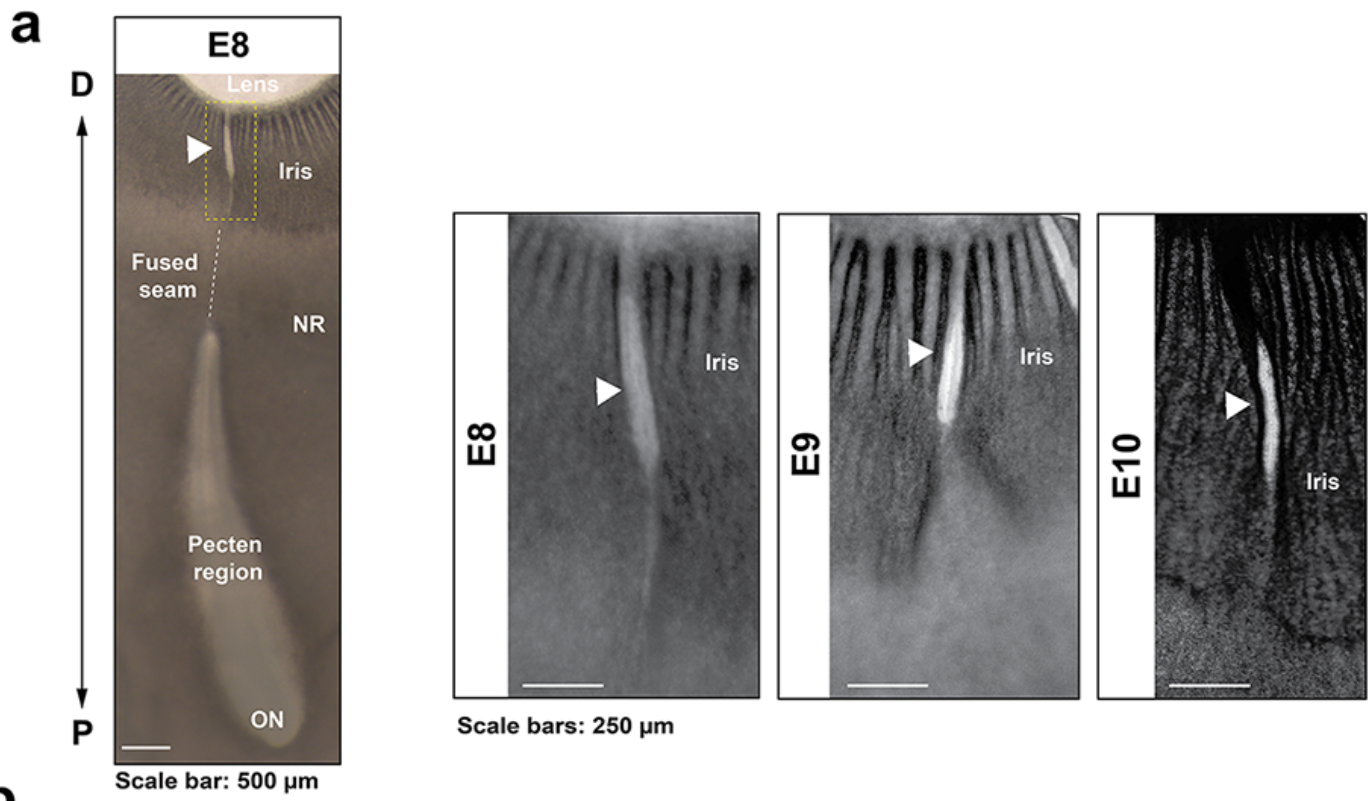
a
E8
D
Lens
Iris
Fused seam
NR
Pecten region
ON
P
Scale bar: 500 µm
E8
Iris
E9
Iris
E10
Iris
Scale bars: 250 µm

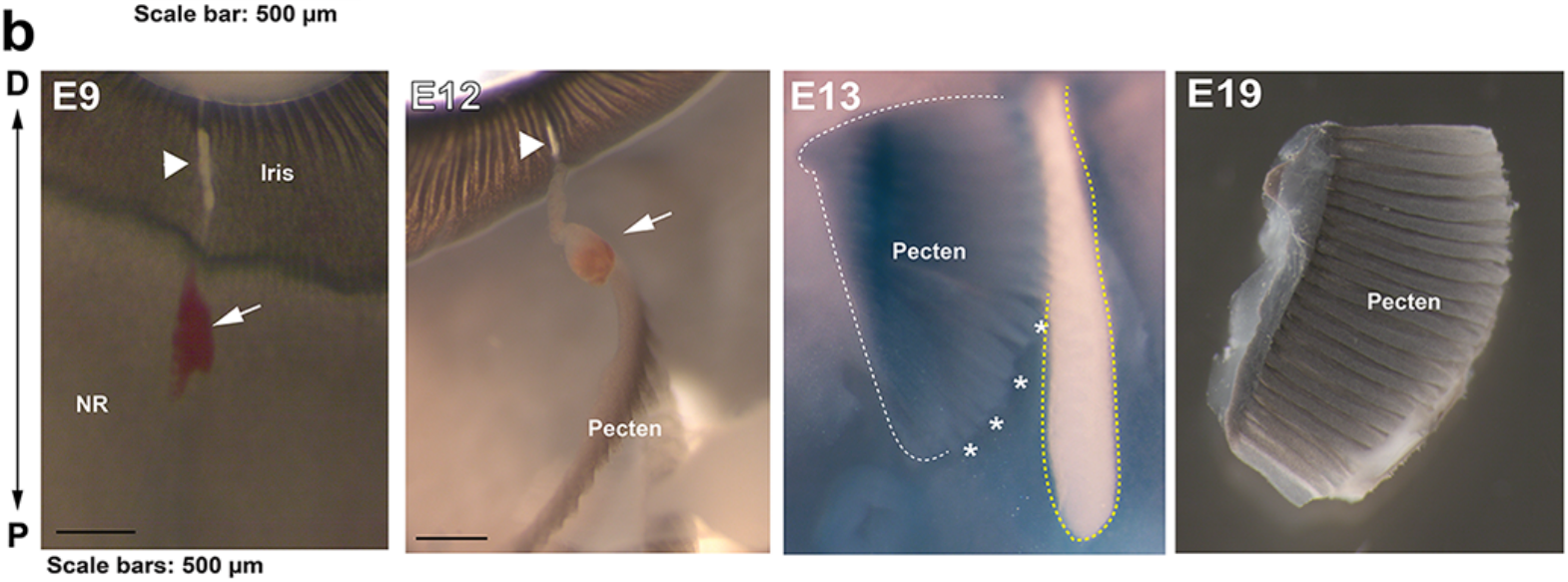
b
D
E9
Iris
NR
P
Scale bars: 500 µm
E12
Pecten
E13
Pecten
E19
Pecten

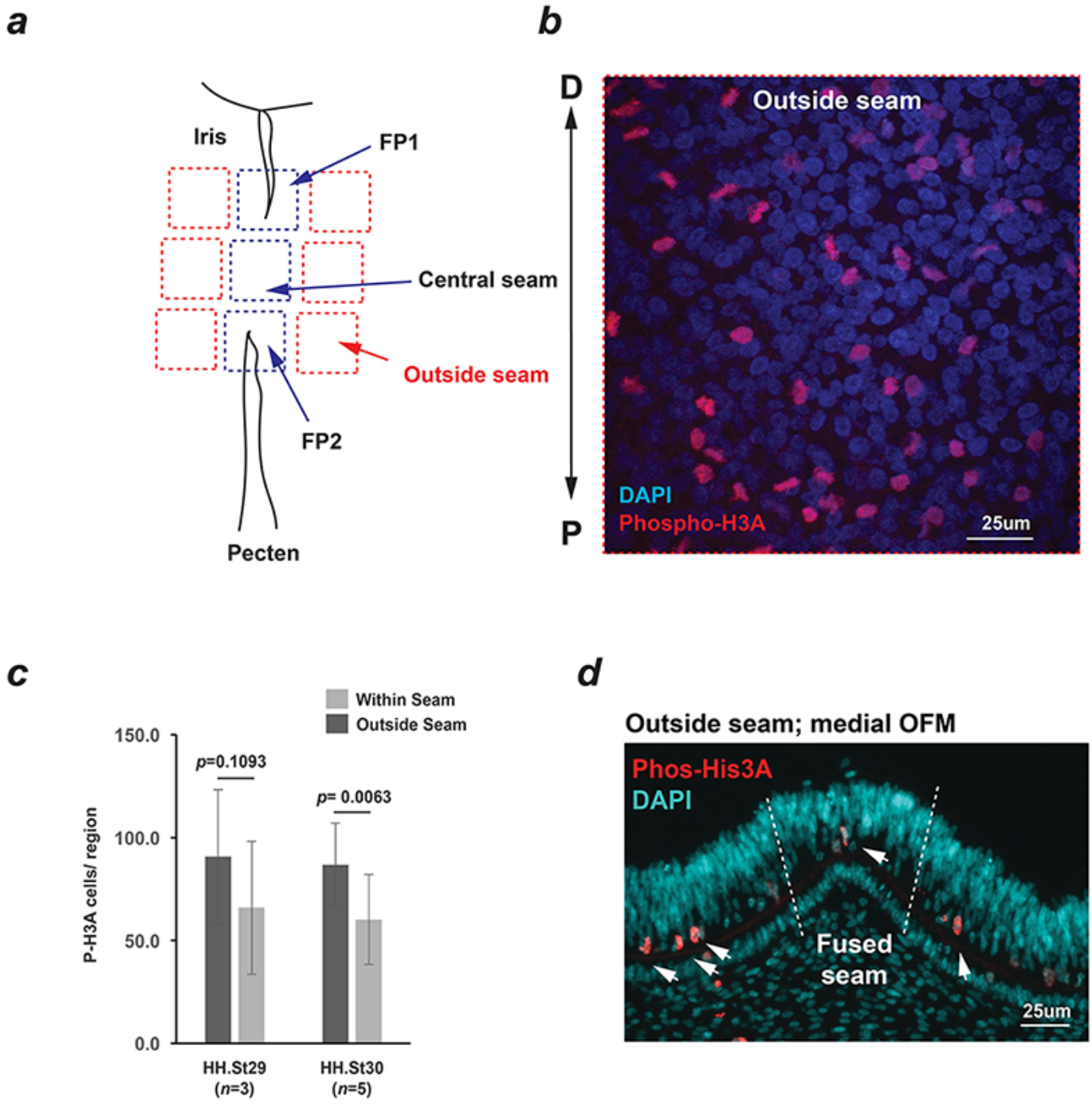
a
Iris
FP1
Central seam
Outside seam
FP2
Pecten
b
D
P
Outside seam
DAPI
Phospho-H3A
25um
c
Within Seam
Outside Seam
150.0
100.0
50.0
0.0
P-H3A cells/ region
p=0.1093
p= 0.0063
HH.St29
(n=3)
HH.St30
(n=5)
d
Outside seam; medial OFM
Phos-His3A
DAPI
Fused
seam
25um

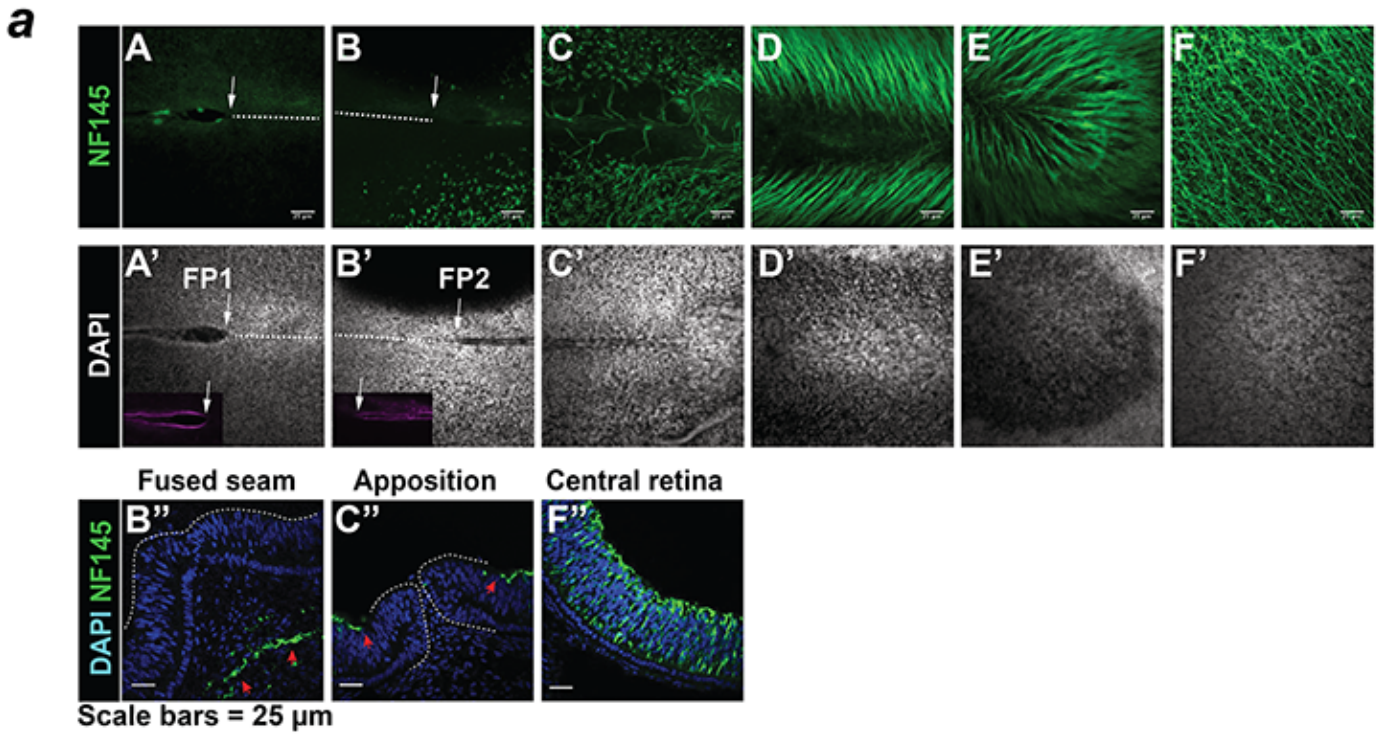
a
NF145
DAPI
A
B
C
D
E
F
A'
B'
C'
D'
E'
F'
FP1
FP2
Fused seam
Apposition
Central retina
DAPI NF145
B''
C''
F''
Scale bars = 25 µm

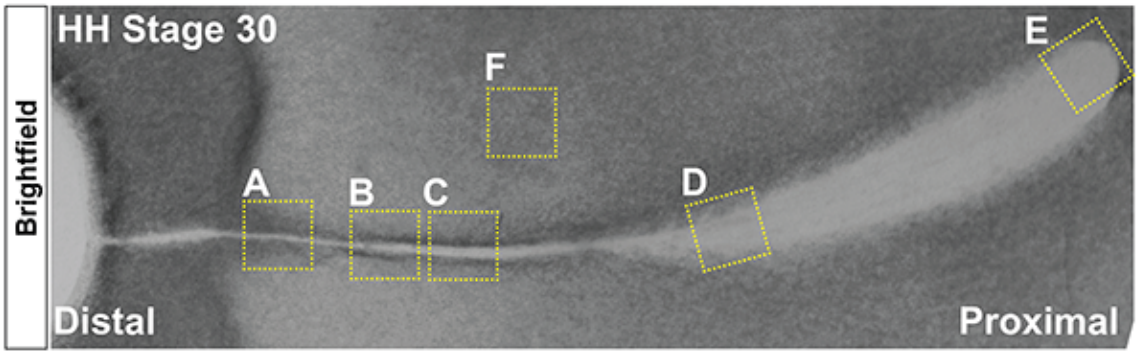
Brightfield
HH Stage 30
A
B
C
D
E
F
Distal
Proximal

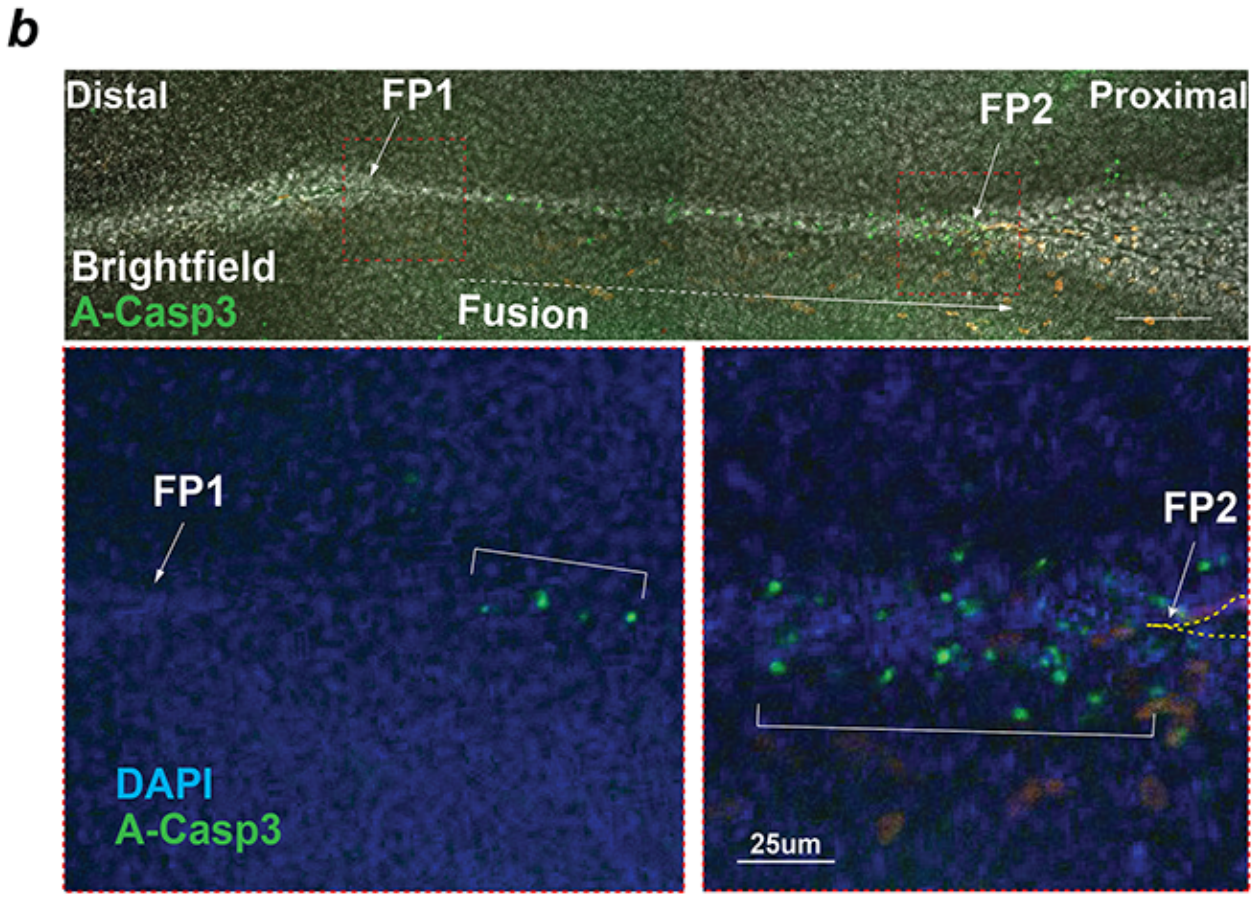
b
Distal
FP1
FP2
Proximal
Brightfield
A-Casp3
Fusion
FP1
DAPI
A-Casp3
FP2
25um

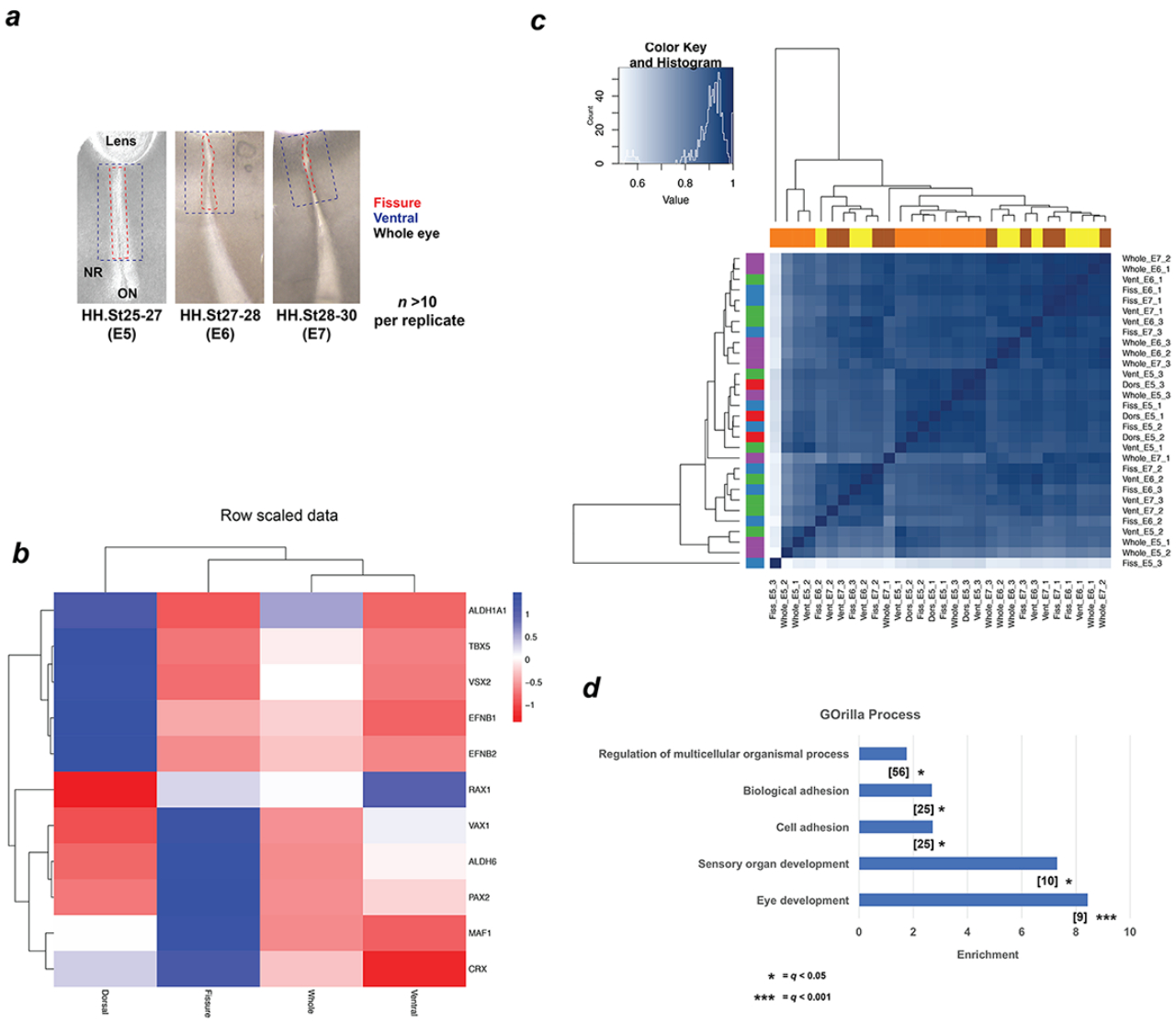
a
Lens
NR
ON
HH.St25-27
(E5)
HH.St27-28
(E6)
HH.St28-30
(E7)
Fissure
Ventral
Whole eye
n >10
per replicate
b
Row scaled data
ALDH1A1
TBX5
VSX2
EFNB1
EFNB2
RAX1
VAX1
ALDH6
PAX2
MAF1
CRX
Dorsal
Fissure
Whole
Ventral
c
Color Key
and Histogram
Count
Value
d
GOrilla Process
Regulation of multicellular organismal process
[56] *
Biological adhesion
[25] *
Cell adhesion
[25] *
Sensory organ development
[10] *
Eye development
[9] ***
Enrichment
* = q < 0.05
*** = q < 0.001

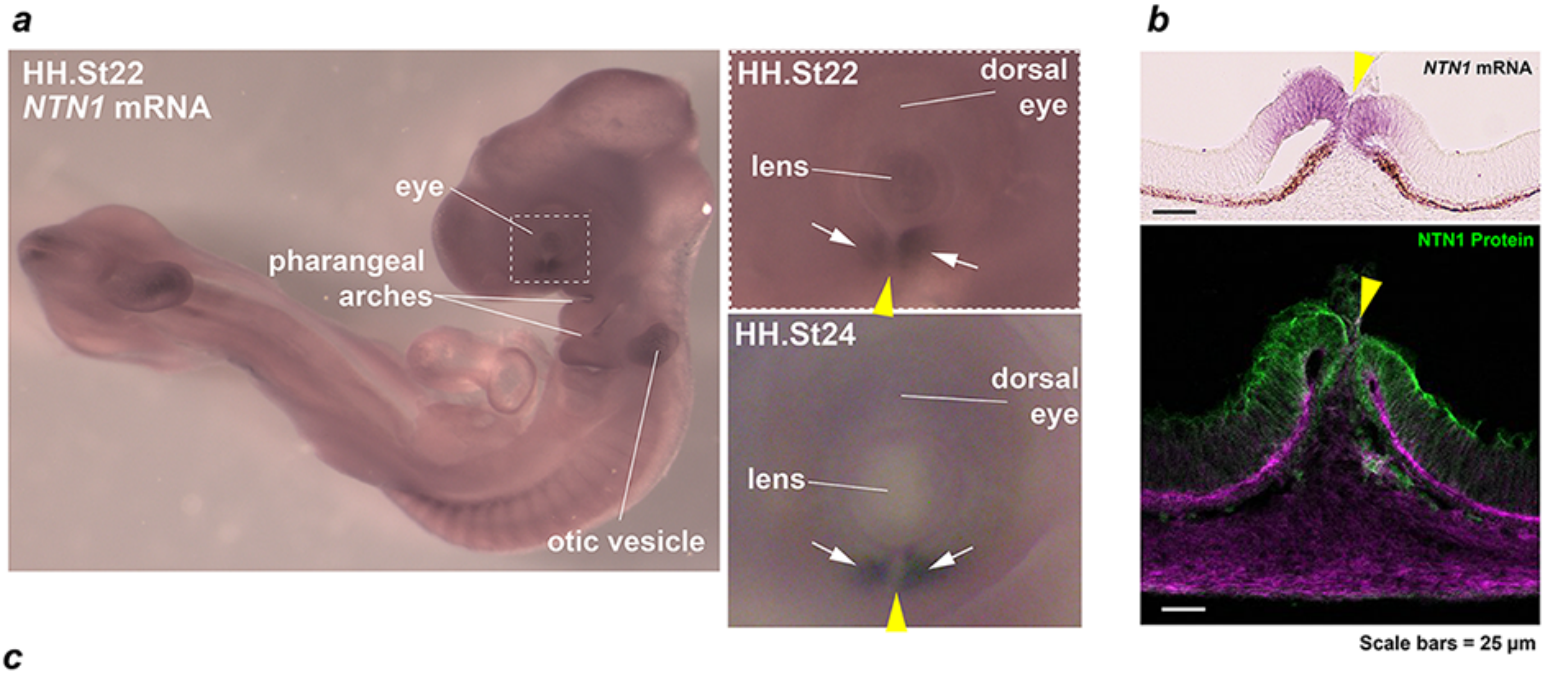
a
HH.St22
NTN1 mRNA
eye
pharangeal
arches
otic vesicle
HH.St22
dorsal
eye
lens
HH.St24
dorsal
eye
lens
b
NTN1 mRNA
NTN1 Protein
Scale bars = 25 µm

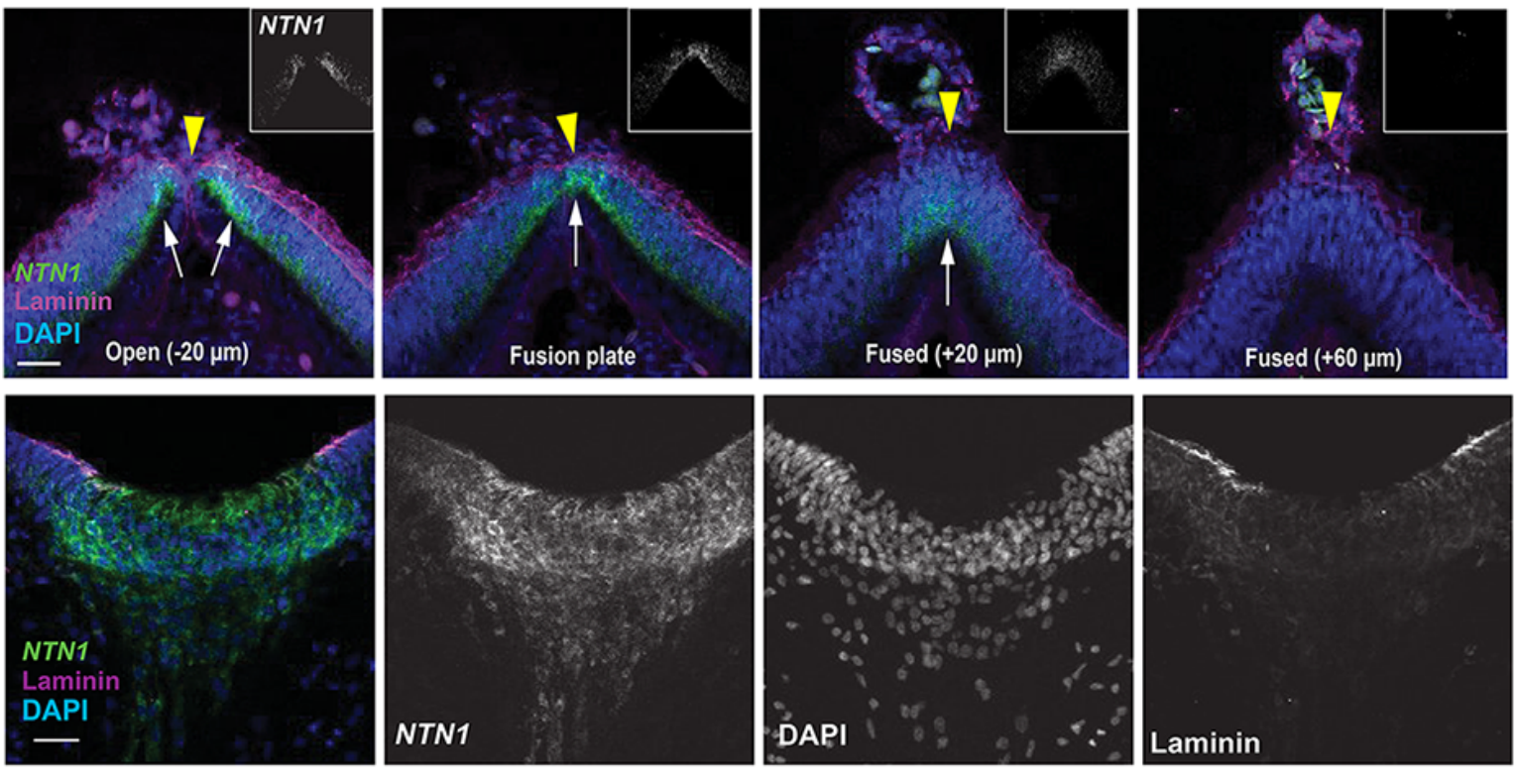
c
NTN1
NTN1
Laminin
DAPI
Open (-20 µm)
Fusion plate
Fused (+20 µm)
Fused (+60 µm)
NTN1
Laminin
DAPI
NTN1
DAPI
Laminin
Scale bars = 25 µm

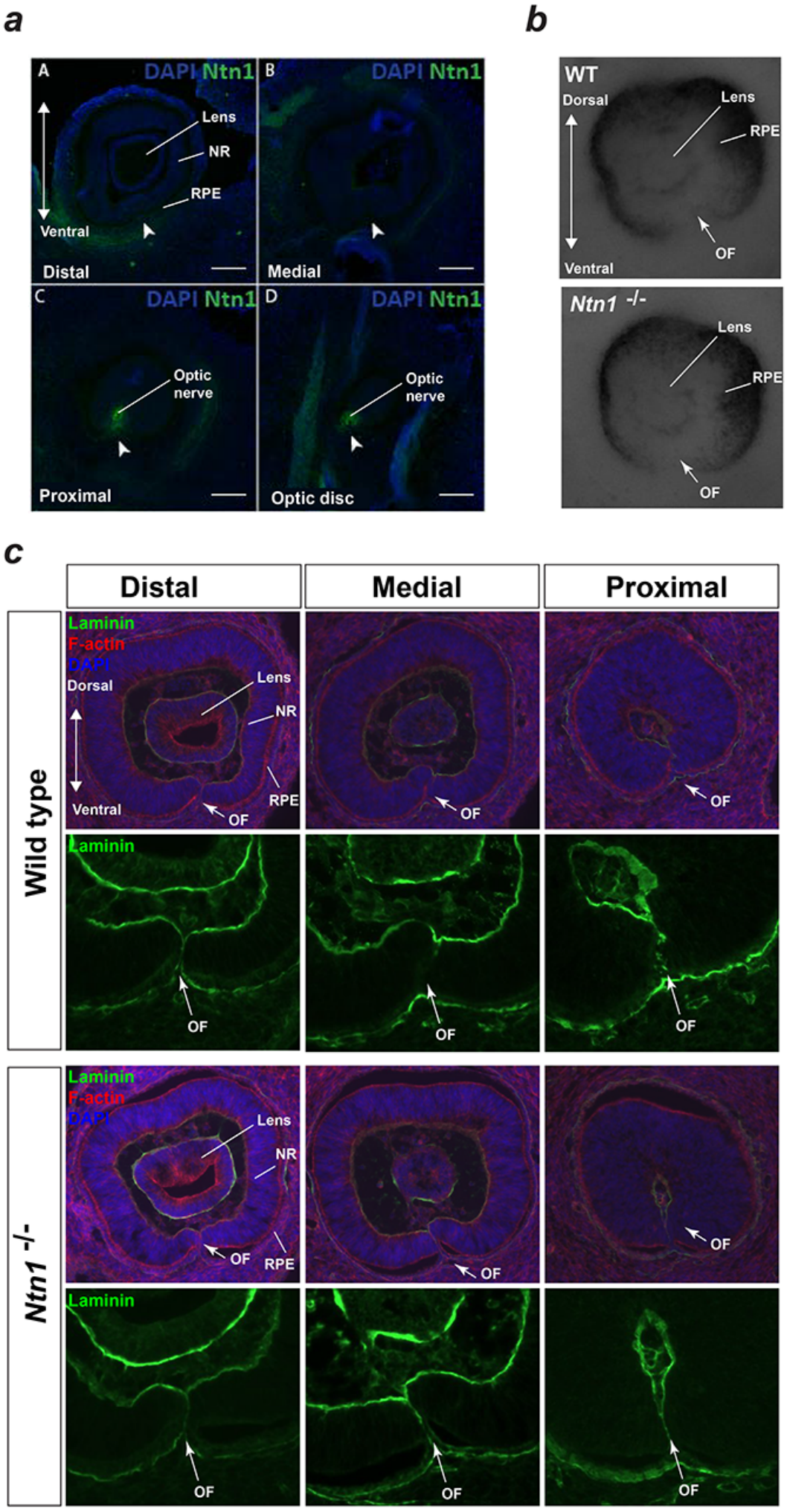
a
A
DAPI Ntn1
Lens
NR
RPE
Ventral
Distal
B
DAPI Ntn1
Medial
C
DAPI Ntn1
Optic nerve
Proximal
D
DAPI Ntn1
Optic nerve
Optic disc
b
WT
Dorsal
Lens
RPE
OF
Ventral
Ntn1 -/-
Lens
RPE
OF
c
Distal
Medial
Proximal
Wild type
Laminin
F-actin
DAPI
Dorsal
Lens
NR
RPE
Ventral
OF
Laminin
OF
Ntn1 -/-
Laminin
F-actin
DAPI
Lens
NR
OF
RPE
Laminin
OF

a

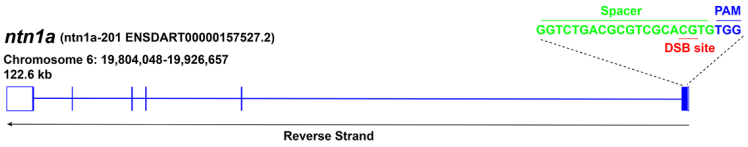

b

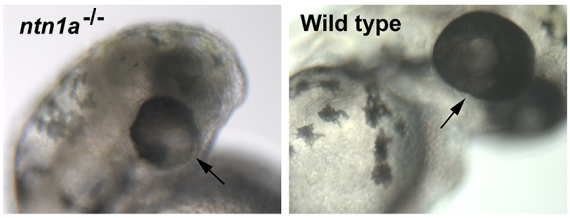

c

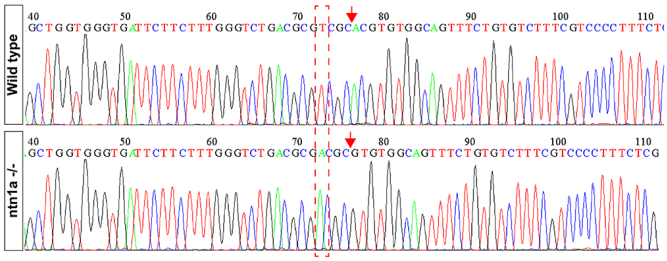

d

Alignment:

```
CLUSTAL O(1.2.4) multiple sequence alignment

WT              MLRVSDALVTLVTLCCVLKGTVGGYGMSMFAAQTSPPDPCYDENGHPRRCIPDFVNAAFG      60
ntn1a-Mutant    MLRVSDALVTLVTLCCVLKGTVGGYGMSMFAAQTSPPDPCYDENGHPRRCIPDFVNAAFG      60
                ************************************************************

WT              KEVRASSTCGKTPSRYCVVTEKGDERHRNCHTCDASDPKKNHPPAYLTDLNNPHNLTCWQ     120
ntn1a-Mutant    KEVRASSTCGKTPSRYCVVTEKGDERHRNAHASRQTQRRITHQLT*--------------     105
                ******************************.*:.  :: : .*  :

WT              SDNYLQYPQNVTLTLSLGKKFEVTYVSLQFCSP      153
ntn1a-Mutant    -----------------------------------    105
```

Translation of mutant allele: *p.Cys90Ala.fs*15*

e

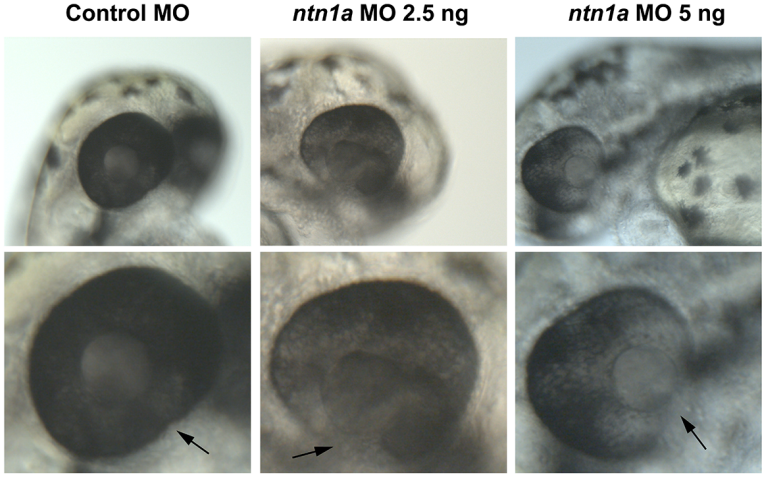

f

ntn1a - CRISPR/Cas9

	WT (*ntn1a* $^{+/+}$)	Heterozygote (*ntn1a* $^{+/-}$)	Homozygote (*ntn1a* $^{-/-}$)
% coloboma (total n)	**0% (0)**	**0% (0)**	**14.3% (3)**
% no ocular phenotype (total n)	**57% (12)**	**28.6% (6)**	**0% (0)**

ntn1a – Morpholino

	Ntn1 MO injected	Control MO injected
coloboma % (total n)	**56.3% (40)**	**0% (0)**
no ocular phenotype % (total n)	**43.7% (31)**	**100% (40)**

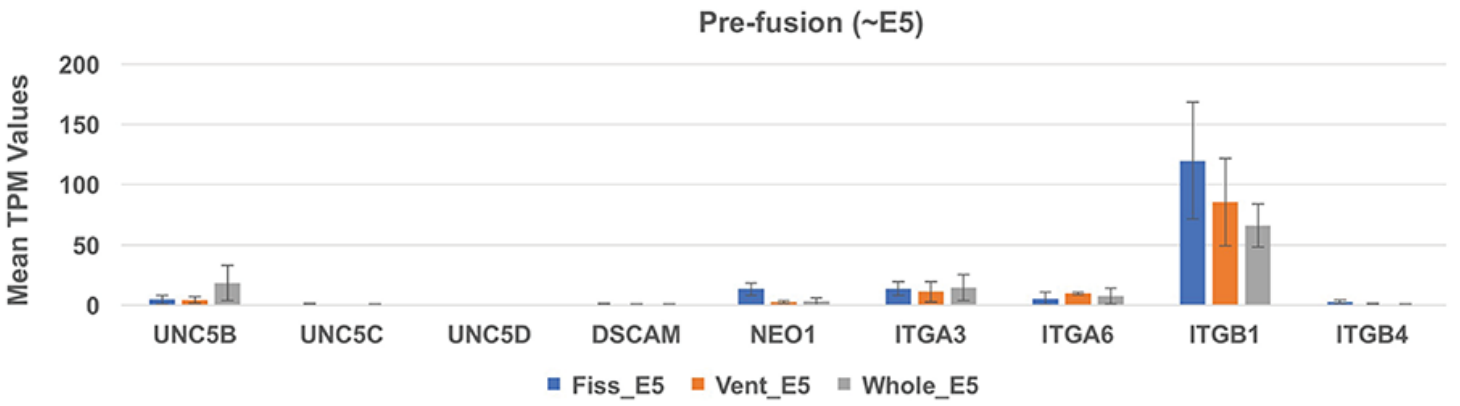
Pre-fusion (~E5)
Mean TPM Values
200
150
100
50
0
UNC5B
UNC5C
UNC5D
DSCAM
NEO1
ITGA3
ITGA6
ITGB1
ITGB4
Fiss_E5
Vent_E5
Whole_E5

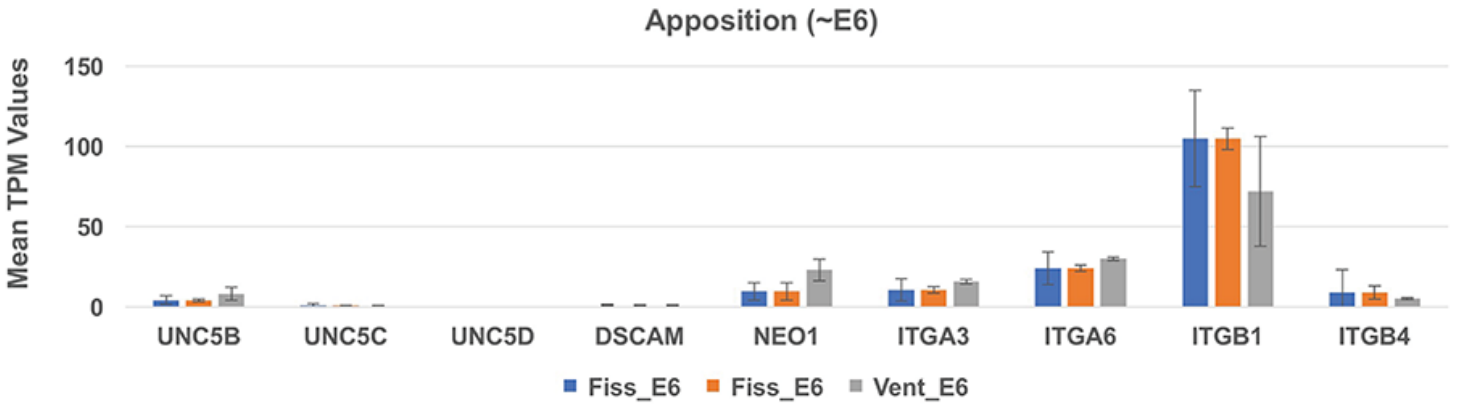
Apposition (~E6)
Mean TPM Values
150
100
50
0
UNC5B
UNC5C
UNC5D
DSCAM
NEO1
ITGA3
ITGA6
ITGB1
ITGB4
Fiss_E6
Fiss_E6
Vent_E6

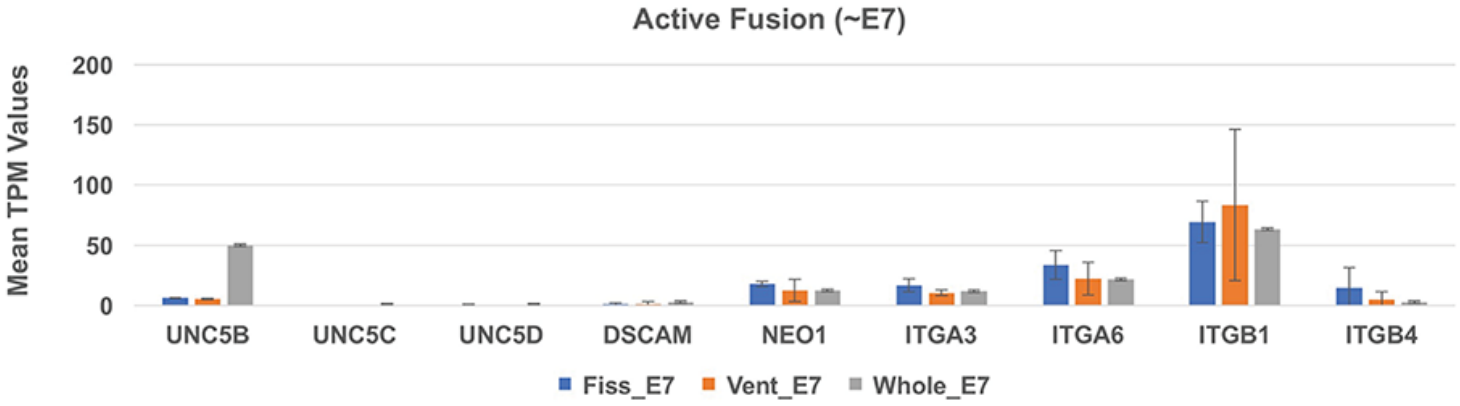
Active Fusion (~E7)
Mean TPM Values
200
150
100
50
0
UNC5B
UNC5C
UNC5D
DSCAM
NEO1
ITGA3
ITGA6
ITGB1
ITGB4
Fiss_E7
Vent_E7
Whole_E7